GEORG-AUGUST-UNIVERSITÄT
GÖTTINGEN

Bachelorthesis

at Max Planck Institute for Dynamics

and Self-Organization Göttingen

Strukturbildung kausalentropisch getriebener Teilchen auf einem Gitter

Pattern formation of causal-entropically driven particles on a lattice

Fritjof Nikolai Vogel

f.vogel@stud.uni-goettingen.de

First reader:	Dr. Marco G. Mazza MPI for Dynamics and Self-Organization Dynamics of Complex Fluids
Second reader:	Prof. Dr. Reiner Kree Georg-August-University Göttingen Institute for Theoretical Physics
Date:	September 16, 2016

Contents

Abstract

A deep connection between intelligence and causal entropy maximization was suggested by Wissner-Gross and Freer in 2013 [1]: intelligence is moving towards a maximization of future possibilities. In this work I use the concept of causal entropic forces to investigate fundamental rules for pattern formation on a lattice. Previously, this has been studied in continuous space and time by Hornischer [2]. I explore three different approaches to calculate the phase-space volume, which is the crucial variable of the causal entropic force: approach A takes the raw number of possible trajectories into account and weights them equally. Here the force is strictly repulsive and the behavior is comparable to an ideal gas. Approach B takes the radius of gyration as a weight for each sampling trajectory to explore the phase space volume. For this approach I find stable patterns, where the appearance ranges from hexagonal to labyrinthine depending on the time horizon and density. Approach C uses the boxcount of each trajectory as its weight. In this approach I find patterns, the appearance depending on time horizon and density but the occurrence also depending on the fraction of explored phase space. If only a small part of the phase space is explored the particles move erratically and no patterns appear.

1 Motivation

What is intelligence? Philosophers, psychologists, sociologist and pedagogues have thought about this questions since time immemorial. Different definitions are discussed in scientific research nowadays, and they include different aspects of intelligence like logic, abstract thought, understanding, self-awareness, communication, learning, emotional knowledge, memory, planning, creativity and problem solving. How intelligence emerged in history is however highly debated. The Darwinian paradigm, where the survival of the fittest applied to intelligence becomes a survival of the fittest and smartest would suggest a continuous increase of intelligence over timescales of hundreds of thousands of years. This, however, is in contradiction with the observation that certain thresholds are passed in time, where a dramatic increase of intelligence was observed. The extragenetic learning system, which determines the intelligence of mammals to a greater extent than the genetically 'prewired' nervous system, evolves on a different time scale. Here only within the lifetime of a living being the learning process exploits the knowledge and wisdom of the environment and of the culture and therefore unfolds the individual intelligence [3]. Human intelligence for example boosted by passing through thresholds originated in abilities described and explained by the human cognitive niche. It is argued that three key abilities are the foundation of human intelligence: the exchange of information through language, the use of tools, and social cooperation [4]. All three abilities act both on the species level and on the individual level, later describes Piaget with a model of four stages [5, 6]. Here I refer to the discourse of Darwin's approach of form to follow function [7] versus D'Arcy Thompson's opposite approach described in Growth and Form [8]. To explore this question it is of fundamental interest to determine what principles are necessary to find phenomena comparable to the human cognitive niche. Finding these principles in non-living particles would set boundaries and suggest a tendency towards similar behavior in systems of living beings [9].

1.1 Structure and pattern formation

Consider social cooperation. One can easily find examples from human activities: buildings, cities, economies, social relationship networks and so on [10]. But also for animals social cooperation can be observed, namely animals living in herds, fish swarms or bird flocks [11]. Reducing complexity and turning away from living beings the vocabulary changes: because the exchange of information is not done through language in the original sense, scientists do not talk about social cooperation but instead call it structure or pattern formation. And when we look around ourselves, there is structure everywhere and at all length scales. This is in apparent contra-

diction with the expectation that any system should exhibit the highest degree of symmetry allowed by the boundary conditions. This state of affairs would represent a thermodynamic equilibrium. Hence, I can conclude that most systems are in a nonequilibrium state. The universe is not a homogeneous blur, it has structure like planets, galaxies and galactic filaments forming a web of unimaginable size [12]. Also on very small length scales there is structure. For example the neuronal system of our brain or the formation of cells [13].

There exist collective structures, which are much more complex than an individual could ever understand, let alone fully controlling. Hence it is necessary to understand what the basic rules which are necessary to find patterns are. For a long time this was usually explained via a top-down implementation process. For example, the queen of a colony of bees or ants gives specific commands and tells all others what to do. Another example would be that the genes in DNA do have the blueprint of their cell and organize the implementation. This top-down approach however reaches its limits at the smallest scale, when the individuals or particles of the system simply cannot have an overview of the whole system. This occurs for example when the complexity of the system exceeds the capacity of comprehension due to limited intelligence. It is simply too hard to imagine something which may possess a blueprint for the universe.

1.2 Causal entropic force

Recently advances in different areas of science research use the principle of causal entropy maximization to explain intelligent behavior. For example in cosmology, where the 'causal entropic principle' was used to compute the expected value of the cosmological constant. Here the entropy of the observers was maximized in a causally connected space-time region [14]. An overview of recent developments in physics, chemistry and biology of the maximum entropy production principle is given by Martyushev and Seleznev [15], where many applications of the principles are listed in detail. More recently, the topic of artificial intelligence has become more and more interesting, because of the rise of computational power. Here also the causal entropy maximization principle gave rise to strategy algorithms which beat human opponents in high look-ahead games like Go or chess [16]. These and other applications of the principle of causal entropy maximization to explain different aspects of intelligent behavior, inspired Wissner-Gross and Freer to propose a deep connection between intelligence and causal entropy maximization in 2013 [1]. Their hypothesis is that intelligence is to move towards more possibilities for the future evolution within a time horizon. This is not only supported by the many examples in nature but also by the fact that applying this principle to simulated particles

shows two important characteristic features of intelligent behavior: tool use and social cooperation.

In this thesis I consider this concept to further evaluate its features of social cooperation and pattern formation. I specifically try to implement this model on a lattice and compare this with existing results for continuous space. If results are comparable this would reduce computational time and result in a simpler algorithmic structure, upon which future work in the field can be based.

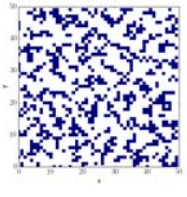

2 Theoretical fundamentals

In this section I derive the causal entropic force in analogy to other generalized forces. Later, I discuss three different approaches to quantify the phase-space volume of the sampling trajectories, which is the crucial variable of the causal entropic force. Approach A considers every realizable trajectory with the same weight, approach B uses the radius of gyration to weigh the trajectories and approach C considers the boxcount of the sampling trajectories as their weight.

2.1 Causal entropic force

In analogy to the systems mentioned in the motivation I work with a physical system far from thermodynamic equilibrium, since the definition of the causal entropic force considers an explicit time dependency. The exact form of this causal entropy, which is maximized through time is derived below.

2.1.1 Theoretical derivation

The causal entropic force is based on the fundamental principle of the Shannon entropy. This entropy originates in information theory and is defined as

$$S(X) = -\sum_{i=1}^{n} \mathrm{P}(x_i) \log_b(\mathrm{P}(x_i)) \ .$$

Here $\mathrm{P}(x_i)$ is the probability of event x_i to occur and $\log_b(\mathrm{P}(x_i))$ is the information content where the base b of the logarithm is in physics typically e. Hence, the entropy is the ensemble mean of the informational content over all events.
The defining property of the causal entropic force is the assumption that intelligence corresponds to maximizing the possibilities of the future evolution of the system. For the exact form three different approaches are explored in this thesis. Approach A considers the number of possible trajectories and therefore maximizes the variety of future evolutions. Approach B maximizes the mean radius of gyration of possible trajectories in each direction and hence maximizes the shift of future evolutions compared to the current state. And approach C maximizes the boxcount and hence maximizes the diversity of future evolutions. The causal entropy is for all three approaches formally defined as

$$S_c(\boldsymbol{X}, \tau) = -k_B \int \mathrm{P}(\mathcal{X}_\tau | \boldsymbol{x}(0)) \ln(\mathrm{P}(\mathcal{X}_\tau | \boldsymbol{x}(0))) \mathcal{D}\mathcal{X}_\tau \ , \tag{1}$$

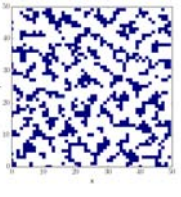

where $\mathrm{P}(\mathcal{X}_\tau|\boldsymbol{x}(0))$ is the probability of the occurrence of trajectory $\mathcal{X}_\tau$ given the starting condition $\boldsymbol{x}(0)$ and τ is the time horizon or number of sampling steps. A schematic explanation is shown in Figure 1, where the evolution of a particle in microstate $\boldsymbol{x}(0)$ is considered and the phase space is explored with random sampling trajectories, which do not pass through the restricted area. For a lattice, the path integral in Eq. (1) lives in a τ^4 dimensional space, and for continuous space in an infinitely dimensional space. From this, I can now define the causal entropic force, in analogy to other generalized forces as

$$\boldsymbol{F_c}(\boldsymbol{X},\tau) = T_c \nabla_{\boldsymbol{x}} S_c(\boldsymbol{X},\tau)|_{\boldsymbol{x_0}} \ . \tag{2}$$

Here T_c is the causal temperature and determines the strength of the causal entropic force. The presence of a spatially constricted region of space generates a force away from it. To quantify the volume of the individual trajectories in very general terms, I consider an open system and integrate over all possible configurations of the system ξ_τ which results in the trajectory $\mathcal{X}_\tau$, and the conditional probability

$$\mathrm{P}(\mathcal{X}_\tau|\boldsymbol{x}(0)) = \int \mathrm{P}(\mathcal{X}_\tau, \xi_\tau|\boldsymbol{x}(0))\mathcal{D}\xi_\tau \ . \tag{3}$$

Putting Eq. (1) and Eq. (2) together I obtain

$$F_j(\boldsymbol{X_0}, \boldsymbol{\tau}) = -T_c k_B \frac{\partial}{\partial q_j(0)} \int \mathrm{P}(\mathcal{X}_\tau|\boldsymbol{x(0)}) \ln\left(\mathrm{P}(\mathcal{X}_\tau|\boldsymbol{x(0)})\right) \mathcal{D}\mathcal{X}_\tau \ ,$$

with q_j the position-space coordinates. From the Lebesgue's dominated convergence theorem it follows that derivation and integral may be swapped

$$F_j(\boldsymbol{X_0}, \boldsymbol{\tau}) = -T_c k_B \int \frac{\partial}{\partial q_j(0)} \left[\mathrm{P}(\mathcal{X}_\tau|\boldsymbol{x(0)}) \ln(\mathrm{P}(\mathcal{X}_\tau|\boldsymbol{x(0)}))\mathcal{D}\mathcal{X}_\tau\right] \ .$$

After using the product rule it becomes

$$\begin{aligned} F_j(\boldsymbol{X_0}, \boldsymbol{\tau}) &= -T_c k_B \int \frac{\partial \mathrm{P}(\mathcal{X}_\tau|\boldsymbol{x(0)})}{\partial q_j(0)} \ln(\mathrm{P}(\mathcal{X}_\tau|\boldsymbol{x(0)}))\mathcal{D}\mathcal{X}_\tau \\ &\quad + \int \mathrm{P}(\mathcal{X}_\tau|\boldsymbol{x(0)}) \frac{\partial \ln(\mathrm{P}(\mathcal{X}_\tau|\boldsymbol{x(0)}))}{\partial q_j(0)} \mathcal{D}\mathcal{X}_\tau \\ &= -T_c k_B \int \frac{\partial \mathrm{P}(\mathcal{X}_\tau|\boldsymbol{x(0)})}{\partial q_j(0)} \ln(\mathrm{P}(\mathcal{X}_\tau|\boldsymbol{x(0)}))\mathcal{D}\mathcal{X}_\tau \\ &\quad + \underbrace{\int \frac{\mathrm{P}(\mathcal{X}_\tau|\boldsymbol{x(0)})}{\mathrm{P}(\mathcal{X}_\tau|\boldsymbol{x(0)})} \frac{\partial \mathrm{P}(\mathcal{X}_\tau|\boldsymbol{x(0)})}{\partial q_j(0)} \mathcal{D}\mathcal{X}_\tau}_{=0} \ . \end{aligned} \tag{4}$$

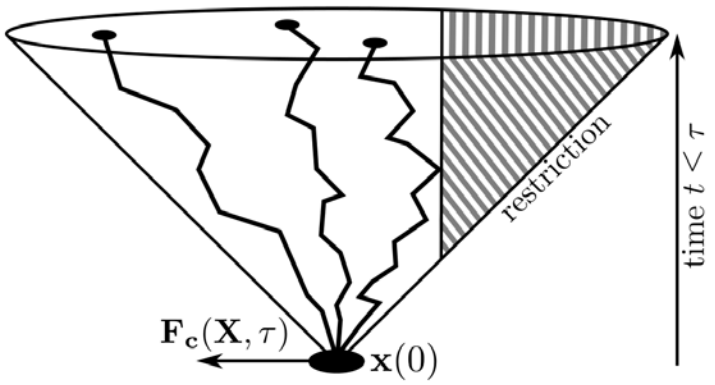

Figure 1: Phase space of a particle in microstate $x(0)$ within time horizon τ. The gray shaded region represents a region of phase space not accessible to the particle. On the right there are no sampling trajectories in the restricted area, so the probability to find trajectories there is zero, which results in a force away from the restriction.

The second term in the last form of Eq. (4) vanishes because Lebesgue integrals are translationally invariant. Because I sample the trajectories with random walks, different steps are uncorrelated. From this it follows that each trajectory can be viewed as a Markov chain and its volume in a multi-dimensional space can be expressed as the product of volumes in each dimension

$$\mathrm{P}(\mathcal{X}_\tau|\boldsymbol{x}(0)) = \left[\prod_{n=1}^{N-1} \mathrm{P}(\boldsymbol{x}(t_{n+1})|\boldsymbol{x}(t_n))\right] \mathrm{P}(\boldsymbol{x}(t_1)|\boldsymbol{x}(0)) \ ,$$

where $N = \tau/\epsilon$, is the total number of steps, and $t_n = n\epsilon$ and ϵ the step length. Computing the derivative of the above probability in position space at time $t = 0$ simplifies to the derivative of the first time step, since all remaining time steps are uncorrelated with the initial step

$$\frac{\partial \mathrm{P}(\mathcal{X}_\tau|\boldsymbol{x}(0))}{\partial q_j(0)} = \left[\prod_{n=1}^{N-1} \mathrm{P}(\boldsymbol{x}(t_{n+1})|\boldsymbol{x}(t_n))\right] \frac{\partial \mathrm{P}(\boldsymbol{x}(t_1)|\boldsymbol{x}(0))}{\partial q_j(0)} \ . \tag{5}$$

The probability gradient of the trajectory from the first step to the second is the same as the negative probability gradient from the second step backwards, namely

$$\frac{\partial \mathrm{P}(\mathcal{X}_\epsilon|\boldsymbol{x}(0))}{\partial q_j(0)} = -\frac{\partial \mathrm{P}(\mathcal{X}_\epsilon|\boldsymbol{x}(0))}{\partial q_j(\epsilon)} \ . \tag{6}$$

For the first sampling step I have to make a choice of how far and what distribution of directions I would like to have. It seems reasonable that the direction is uniformly distributed and the probability decays to zero, because of the presence

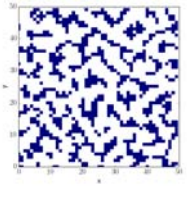

of the horizon, so that information gathered about the environment, is a local and continuous quantity. I choose a distribution where all directions with step length one are considered as well as the position of the particle itself.

$$\begin{aligned}\mathrm{P}(\mathcal{X}_\epsilon|\boldsymbol{x}(0)) &\sim \begin{cases} 1/5 & : \text{first neighbor or particle's position} \\ 0 & : \text{else} \end{cases} \\ &= \mathrm{H}(|\boldsymbol{x}| - 1) \ ,\end{aligned}$$

with $\mathrm{H}(x)$ the Heaviside step function. With this choice, the derivative becomes then

$$\begin{aligned}&\frac{\partial \mathrm{P}(\mathcal{X}_\epsilon|\boldsymbol{x}(0))}{\partial q_j(\epsilon)} = f_j(0)\mathrm{P}(\mathcal{X}_\epsilon|\boldsymbol{x}(0)) \\ &\text{with } f_j(0) = \delta(|\boldsymbol{x}| - 1) \\ &\text{and } \langle f_{j,n}\rangle_n = 0 \ ,\end{aligned} \tag{7}$$

with the $\delta(x)$ the Kronecker delta function. However, other distributions can also be considered, for example a Gaussian distribution for the first step's length.
To further simplify Eq. (5), I insert Eq. (7) into Eq. (6) and obtain

$$\begin{aligned}&\frac{\partial \mathrm{P}(\mathcal{X}_\epsilon|\boldsymbol{x}(0))}{\partial q_j(0)} = -f_j(0)\mathrm{P}(\mathcal{X}_\epsilon|\boldsymbol{x}(0)) \\ \Rightarrow &\frac{\partial \mathrm{P}(\mathcal{X}_\tau|\boldsymbol{x}(0))}{\partial q_j(0)} = -\left[\prod_{n=1}^{N} \mathrm{P}(\mathcal{X}_\epsilon|\boldsymbol{x}(t_n))\right] f_j(0)\mathrm{P}(\mathcal{X}_\epsilon|\boldsymbol{x}(0)) = -f_j(0)\mathrm{P}(\mathcal{X}_\tau|\boldsymbol{x}(0))\end{aligned}$$

This finally leads to an expression for the causal entropic force

$$F_j(\boldsymbol{X_0}, \boldsymbol{\tau}) = -T_c k_B \int f_j(0)\mathrm{P}(\mathcal{X}_\tau|\boldsymbol{x}(0)) \ln[\mathrm{P}(\mathcal{X}_\tau|\boldsymbol{x(0)})]\mathcal{D}\mathcal{X}_\tau \ . \tag{8}$$

2.1.2 Discretization of causal entropic force

I am interested in applying the methods of the previous section to a square lattice in two dimensions. For that I introduce a measure for the volume of a trajectory

$$\Omega_n = \frac{1}{M\mathrm{P}(\mathcal{X}_{\tau,n}|\boldsymbol{x}(0))} \ ,$$

where M is the number of sampling trajectories. Here I assume that within a neighborhood of a sampled trajectory the volume does not vary significantly and therefore I can assume a uniform probability distribution. In addition I normalize

the probability with

$$\sum_{n=1}^{M} \Omega_n \mathrm{P}(\mathcal{X}_{\tau,n}|\boldsymbol{x}(0)) = 1 \; .$$

From this I can now rewrite Eq. (8) for a discrete sampling phase space

$$F_j(\boldsymbol{X}_0, \tau) = -\, T_c k_B \sum_{n=1}^{M} f_{j,n}(0) \frac{1}{M\Omega_n} \ln\left(\frac{1}{M\Omega_n}\right) \Omega_n \tag{9}$$

I also used the fact that the phase-space volume Ω_n is not only a measure for the phase-space trajectories but also an approximate measure of the distances between the trajectories in a close neighborhood of the trajectories $\mathcal{D}\mathcal{X}_\tau \approx \Omega_i$. In general the system could evolve towards a different ergodic component depending on the distribution of the initial force $f_j(0)$. This however is not taken into account here. Rearranging Eq. (9) gives

$$F_j(\boldsymbol{X}_0, \tau) = \frac{T_c k_B}{M} \left[\underbrace{\sum_{n=1}^{M} f_{j,n}(0) \ln(M)}_{=0} + \sum_{n=1}^{M} f_{j,n}(0) \ln(\Omega_n) \right] \; . \tag{10}$$

The first sum vanishes because the average over all initial forces vanishes $\langle f_{j,n} \rangle = 0$, where n is the number of sampling trajectories. For small variations around $\Omega_n = 1$ a series expansion of Eq. (10) becomes

$$F_j(\boldsymbol{X}_0, \tau) \approx \frac{T_c k_B}{M} \left[\sum_{n=1}^{M} f_{j,n}(0) \Omega_n \right] \; . \tag{11}$$

Since the length of the steps are chosen in order to be restricted to one the normalization of the force in Eq. (11) is arbitrary and the change of position of the particle for a timestep becomes

$$\boldsymbol{x}_j(t+1) = \boldsymbol{x}_j(t) + \boldsymbol{e} \quad \text{with} \quad \boldsymbol{e} = \mathrm{argmax}[\langle \Omega_{n_d} \rangle_{n_d}]_d \; , \tag{12}$$

where n_d are all sampling trajectories starting from one of the five fields and the average is taken for all phase space volumes of all sampling trajectories starting from one specific field. The argmax function returns the vector of length 1 of the direction of the maximum average phase space volume starting from this lattice site.

For the phase-space volume of the different sampling trajectories different approaches can be considered. The simplest would be to weigh each trajectory equally.

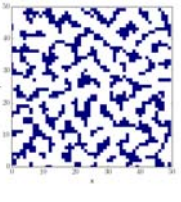

This results in a measure for the causal entropic force as the number of trajectories which exist in a certain direction (approach A). Another approach would be to weigh each trajectory with the radius of gyration (B), a measure for the elongation of trajectories, or similar to take the boxcount of a sampling trajectory as its measure (C), which is a method of quantifying their occupied space.

In this thesis I examine these three approaches, but different approaches are also possible, for example using the displacement of a sampling trajectory.

2.1.3 Approach A: Number of trajectories

The number of possible trajectories for one particle moving freely on an infinite two-dimensional lattice within a time horizon τ is 4^τ, since there are four directions and τ time steps to consider. This number is reduced by any obstacles within the particle's horizon, such as walls or other particles. The number of possible trajectories from the neighboring four points are then used as a measure for the causal entropic force. We define

$$\Omega_{A,n}(\mathcal{X}_\tau) = \begin{cases} 0 : \text{obstacle in the trajectory} \\ 1 : \text{else} \end{cases}$$
$$\overset{(12)}{\Rightarrow} \boldsymbol{e} = \text{argmax}\left[\text{number of trajectories in direction d}\right]_d \ .$$

This method is implemented iteratively in terms of τ. Starting with the last step I count all accessible neighboring fields for every point on the lattice. Next, for the second last step the particle can move to the neighboring fields and from there has one more step, this however I already calculated in the previous step. So I take the numbers of possibilities in the neighboring fields of a lattice site for one remaining step and sum them up for all lattice sites. This represents now the number of possibilities for two remaining steps (see Figure 2). I repeat this process of summation of the neighboring field's possibilities until I reach the desired τ value.

If the particles collide they experience a hard-sphere potential, so two particles cannot be at the same lattice site. To sum up: The particle gathers information about its environment and moves more likely in the direction of more available options.

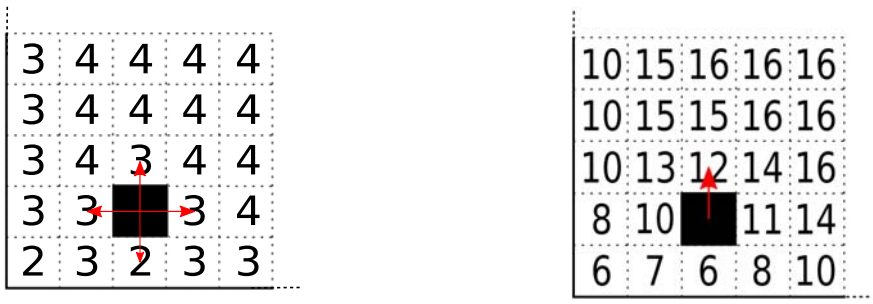

Figure 2: Counting the possible trajectories of a particle near a corner using a recursive method: at first calculate all possibilities for the last step from every lattice site, i.e. one for every neighboring lattice site which is not blocked by a wall or other particles (left panel). Then for the second last step add the numbers of the last step of the neighboring fields to receive the number of possibilities for the two last steps (right panel). Now iterate the calculation until the number of steps equals the given τ.

2.1.4 Approach B: Radius of gyration

The second approach to quantify the phase-space volume is the radius of gyration

$$\Omega_{\mathrm{B,n}}(\mathcal{X}_\tau) = R^2_{\mathrm{gyr},i} = \frac{1}{\tau}\sum_{t=1}^{\tau}(\boldsymbol{r}_t - \boldsymbol{r}_{\mathrm{mean}})^2$$

Here τ is again the time horizon of the particle, $\boldsymbol{r}_t$ is the position of a particle along a sampling trajectory and $\boldsymbol{r}_{\mathrm{mean}}$ its mean over all timesteps of one specific sampling trajectory. For a schematic image of the calculation of the radius of gyration for a random walk on a discrete lattice see Figure 3. From this follows that more elongated trajectories have a bigger radius of gyration and consequently represent a larger contribution to the causal entropic force.

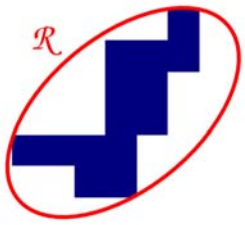

Figure 3: Schematic explanation of the radius of gyration

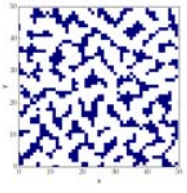

2.1.5 Approach C: Boxcount

The third approach I use is to weigh the sampling trajectory with its boxcount, a schematic explanation is shown in Figure 4. This approach is an elegant way to use the lattice topology also to quantify the phase space.

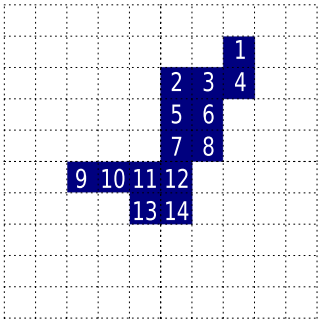

Figure 4: Schematic explanation of the boxcount $\Omega_{\text{box}} = 14$ of a trajectory with length $\tau = 20$

Approach C is similar to approach B. In Figure 5 for every possible trajectory with time horizon $\tau = 9$ the radius of gyration and boxcount are calculated and plotted (small dots). To show the trend the radius of gyration for one value of the boxcount is averaged, which is indicated by the line. This is done for $\tau = 9$. It shows that for a small number of self-crossings of the sampling trajectory, i.e. for higher values of boxcount, the correlation between radius of gyration and boxcount is linear, but with increasing self-crossings, hence decreasing boxcount of a trajectory the weight of the radius of gyration decreases more rapidly than the boxcount, since the slope decreases with decreasing boxcount. To sum up, the radius of gyration weights the short trajectories less than the boxcount, for long trajectories the two approaches B and C are linearly correlated.

To compare the approach A with the two approaches B and C, we see that in the first the number of possibilities is maximized and hence the variety of future evolutions. The approach B and C however tries to maximize the radius of gyration and boxcount, respectively, and therefore maximizes the possibility to shift in future evolutions compared to the current state and the diversity of future evolutions, respectively.

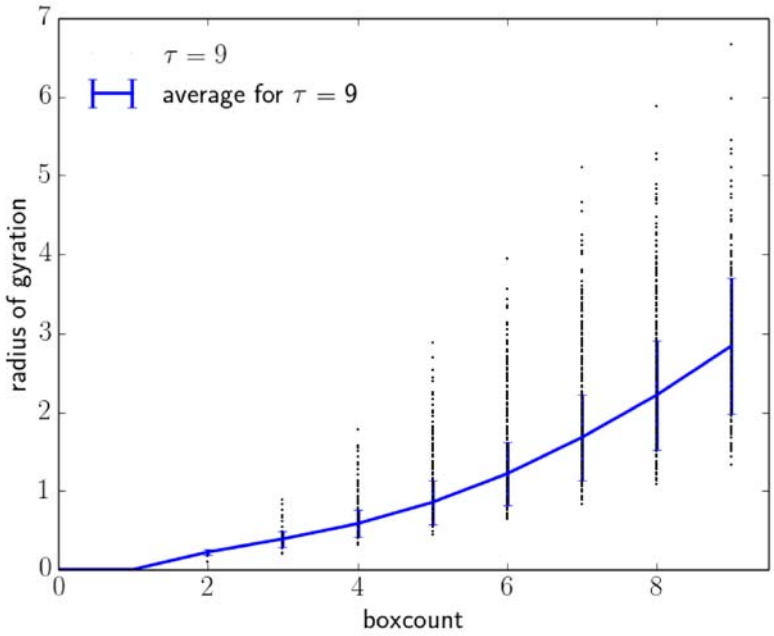

Figure 5: Correlation between boxcount and radius of gyration. It shows that for small number of self-crossings, i.e. high boxcount, of a sampling trajectory the correlation is linear. For an increasing number of self-crossings of the sampling trajectory, the boxcount decreases linear, the radius of gyration however decreases more rapidly. As a result the approach B weights the shorter trajectories less than approach C.

2.2 Pattern formation

In this section I discuss the Swift-Hohenberg model as a simple model to develop a theoretical understanding of the necessary ingredients to find hexagonal and stripe patterns from nonlinear instabilities. I follow the explanation in Cross and Greenside [17]. Before doing that I introduce basic ideas such as growth rate and types of instabilities.

Starting with a two dimensional system of infinite size, and hence translational invariant, the stationary uniform evolution of small perturbations of the nonequilibrium system are linearized by considering a single simple Fourier mode of the form

$$u(x,t) = e^{\sigma_{\boldsymbol{q}} t} e^{i\boldsymbol{q}\cdot\boldsymbol{x}} \tag{13}$$

where $\boldsymbol{x}$ is the in-plane direction and $\boldsymbol{q}$ the wave vector, which grows exponentially with a complex growth rate $\sigma_{\boldsymbol{q}}$ depending on the wave vector $\boldsymbol{q}$. For non-uniform or not translational invariant systems superposition of the single Fourier solutions are the solutions, however then no single and simple growth rate can be extracted.

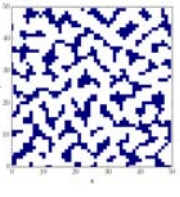

Linear stability is given for a uniform state if the real part of the growth rate Re $\sigma_{\boldsymbol{q}}$ is negative for all wave vectors $\boldsymbol{q}$. When changing a parameter p a bifurcation may occur when the first Re $\sigma_{\boldsymbol{q_c}}$ becomes positive at the critical parameter p_c. Here small pertubations of the system do not decay to zero, but instead increase exponentially and that mode becomes unstable. The imaginary part of the growth rate is $\omega_c = -\text{Im } \sigma_c$ the oscillatory frequency, if this is zero the solution is called stationary, else oscillatory.

The way the growth rate depend on the wave vector $\boldsymbol{q}$ determines the type of instability [18]. For stationary solutions there are three types of instabilities distinguished. The first is type I instability where the real part of the growth rate Re $\sigma_{\boldsymbol{q}}$ varies smoothly around $\boldsymbol{q_c}$ as a quadratic function (see Figure 6). Introducing a reduced control parameter $\epsilon = \frac{p}{p_c} - 1$, the growth rate becomes $\sigma_{q_c}(\epsilon = 0) = 0$. Expanding for small ϵ gives

$$\sigma_{q_c} \approx \frac{\epsilon}{T_0} \ , \tag{14}$$

where T_0 is a characteristic time scale of the instability. Here it was assumed that the growth rate depends linear on the control parameter, which is called the transverse assumption in bifurcation theory. Expanding now around the other parameter for small fluctuations around the wave number $q = q_c$ gives

$$\sigma_q(p = p_c) \approx -\frac{\xi_0}{T_0}(q - q_c)^2 \ , \tag{15}$$

where ξ_0 is the coherence length, which determines a length scale in with small perturbations change the state of the system.
Combining Eq. (14) and Eq. (15) gives the linearized behavior of the growth rate σ_q around $q = q_c$ and $p = p_c$.

$$\sigma_q \approx \frac{1}{T_0}\left[\epsilon - \xi_0^2(q - q_c)^2\right] \ . \tag{16}$$

For type II the growth rate $\sigma_{\boldsymbol{0}} = 0$ and for a parameter $p > p_c$ the $\sigma_{\boldsymbol{q}}$ has a maximum at $\boldsymbol{q} \neq 0$ (see Figure 7). For type III the growth rate decays quadratic and has its maximum at $\boldsymbol{q} = 0$ for all values of the parameter p (see Figure 8).

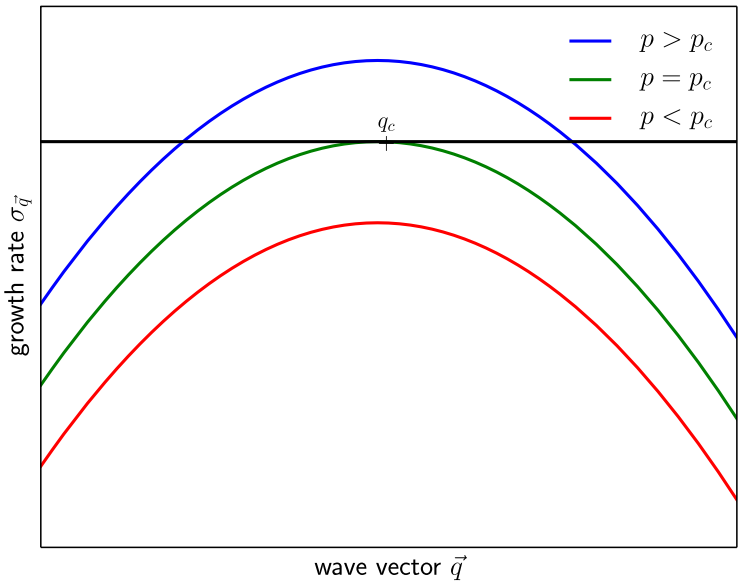

Figure 6: Type I instability: growth rate $\sigma_{\boldsymbol{q}}$ varies quadratic around $\boldsymbol{q_c}$

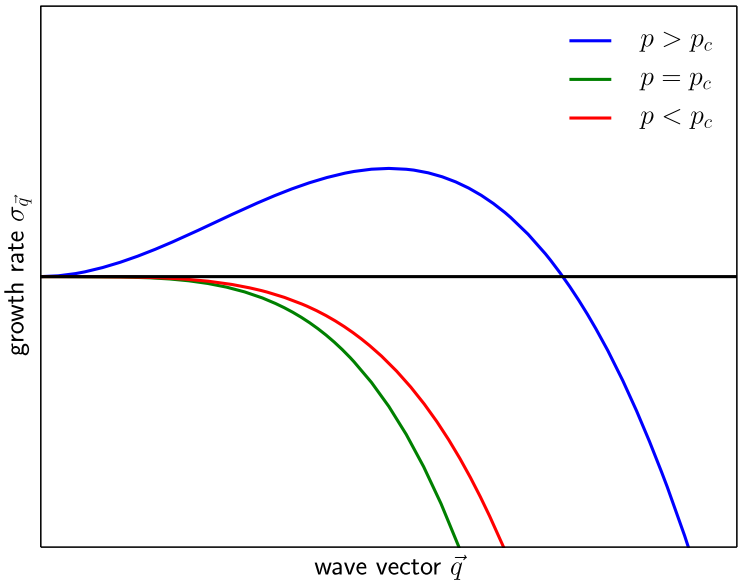

Figure 7: Type II instability: growth rate $\sigma_{\boldsymbol{q}}$ varies quadratic around $\boldsymbol{q_c}$

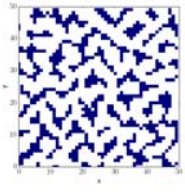

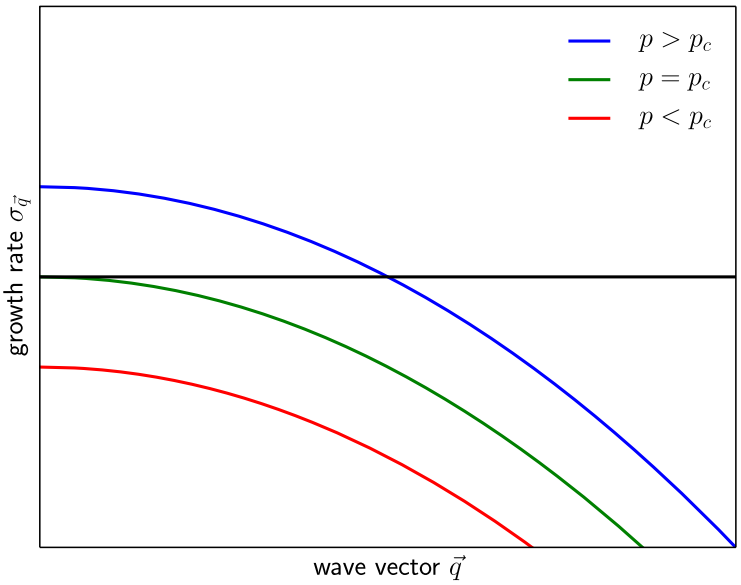

Figure 8: Type III instability: growth rate $\sigma_{\boldsymbol{q}}$ varies quadratic around $\boldsymbol{q_c}$

2.2.1 Swift-Hohenberg model

The Swift-Hohenberg model is one of the simplest models, where stripe and hexagonal patterns can be observed. In the following I give a heuristic derivation before discussing properties and the potential of the model.

I start with a uniform and rotationally invariant system in a two dimensional plane, and further assume a type I instability. The growth rate can only depend on the magnitude of the wave vector $\boldsymbol{q}$ and not on its orientation; the first order expansion of the growth rate gives

$$\sigma_{\boldsymbol{q}} \approx p - c(q - q_c)^2. \tag{17}$$

Asuming small variations around the critical wave number $q + q_c \approx 2q_c$ gives us

$$\sigma_{\boldsymbol{q}} \approx p - c\left(\frac{q + q_c}{2q_c}\right)^2 (q - q_c)^2 \approx p - \frac{c}{4q_c}(q^2 - q_c^2)^2. \tag{18}$$

We can now multiply Eq. (13) with Eq. (18) and rewriting $\sigma_{\boldsymbol{q}} u = \partial_t u$ and $q^2 u = (-\nabla^2)u$ gives us

$$\partial_t u = ru - \left(\nabla^2 + 1\right)^2 u$$

where $1 = \frac{c}{4q_c}$ and $q_c = 1$ were chosen and $r \propto p$ so that constant factors were

eliminated. Here the growth rate $\sigma_{\boldsymbol{q}} = r - (q^2 - 1)^2$ needs to be corrected so that finite solutions may occur, rather than continuously growing solutions. The cubic term is the lowest order term which maintains the inversion symmetry and reduces the growth rate. So the Swift-Hohenberg model is given by the form:

$$\partial_t u = ru - \left(\nabla^2 + 1\right)^2 u - u^3 \,. \tag{19}$$

Boundary conditions are usually given by the equations

$$u = 0 \text{ and } (\hat{\boldsymbol{n}} \cdot \nabla) u = 0 \tag{20}$$

where $\hat{\boldsymbol{n}}$ is the normal vector at the boundaries.

Examining now the dynamics of the Swift-Hohenberg model an important property is that it has a potential, which is called a Lyapunov functional of the field u, which decreases monotonically with time. Analogies would be the total energy of a frictionally damped pendulum or the free energy of a thermodynamic system near equilibrium. However, the dynamics ceases after a transient time in some local minimum of this potential, which shows pattern formation of some type. This minimum depends on initial conditions and the values of the parameter. I define the potential of Eq. (19) with boundary conditions (20) as

$$V = \int\int dxdy \left(-\frac{1}{2} r u^2 + \frac{1}{4} u^4 + \frac{1}{2} \left[\left(\nabla^2 + q \right) u \right]^2 \right) \tag{21}$$

Time derivaties on both sides of Eq. (21) gives

$$\frac{dV}{dt} = \int\int dxdy \left(\left(-ru + u^3 \right) \partial_t u + \left[\left(\nabla^2 + 1 \right) u \right] \left[\left(\nabla^2 + 1 \right) \partial_t u \right] \right) \tag{22}$$

Integrating twice by parts the term $\left[\left(\nabla^2 + 1 \right) u \right] \nabla^2 \partial_t u$ - where the surface terms vanish for boundary conditions of (20) and periodic boundaries as well - gives

$$\frac{dV}{dt} = \int\int dxdy \left(\left[-ru + u^3 + \left(\nabla^2 + 1 \right)^2 u \right] \partial_t u \right) \overset{(19)}{=} - \int\int dxdy (\partial_t u)^2 \,. \tag{23}$$

Since integrating non-negative terms gives always non-negative results the integral is always non-negative and the derivative is always non-positive, hence it is shown that the potential decreases monotonically in time. Which local minimum of the potential is reached after a transient time however depends on the initial condition and the explicit form of the potential. A schematic form of the potential in Figure 9 illustrates that different minima correspond to different appearances of the patterns and in general there is a potential barrier between these minima.

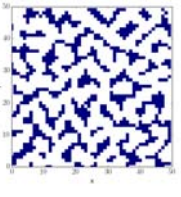

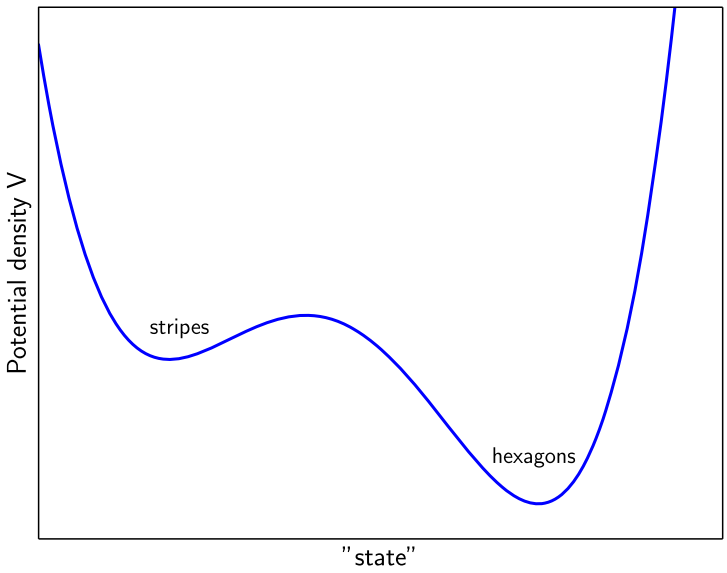

Figure 9: Schematic potential of the Swift-Hohenberg model, with different minima corresponding to different appearances of the pattern seperated by a potential barrier.

Numerical simulations show that for the Swift-Hohenberg model indeed stripe and hexagonal patterns are observed. The results of the Swift-Hohenberg model and of the causal entropically driven particles are not intended to be comparable in quantitative detail. However, a deeper understanding is gained by reproducing qualitatively similar results with a different model and comparing the two theoretical frameworks.

3 Approach A: Causal entropic force

In this section I explain my findings for the approach A as a way to measure the phase-space volume. Firstly in section 3.1, I examine a two and three particle system in free space; then in section 3.2, I consider many particle systems with periodic boundary conditions, which I call free space for simplicity. Finally, I describe the effect of walls, firstly as confinement in a simple box in section 3.3 and secondly in a bottleneck with varying neck's lengths in section 3.4.

3.1 Particle interaction

As a foundation for describing the more complex processes which involve many particles and particle-wall interactions, it is necessary to understand the simplest case of two particles interacting in free space. Figure 10a shows the number of possible trajectories starting from each lattice site. It becomes evident that the number of possibilities is reduced by the presence of the other particle, as a consequence the number of possibilities away from the other particle is higher than towards it. This results in a net repulsive force. This is true for all time horizons τ and all distances between the particles, which are smaller than the time horizon.

Previously line patterns where found. To test this I examined a three particle system and check if there is an inward force to form a lane. Within approach A particles always interact repulsively, as seen in Figure 10b. For the middle particle at position (51,50) the in-lane number of possibilities at (50,50) are smaller than the number of possibilities away from the other particles at (52,50). As a consequence, this results in a maximum distance between the particles and no lane formation can be observed. From this examination it follows that approach A is qualitatively equivalent to a repelling potential (see Figure 11). As a consequence a homogeneous distribution of particles is expected after a transient time.

3.2 Free space

Turning to many-particle systems in free space the particles reach a steady state within a time of the order $t_{\max} = 100$. Depending on the method of implementation this effect is more or less rapid. For example if one considers the number of options of movement (four directions plus the possibility to remain in the same lattice site) as a relative probability to move to these fields the transient time is longer than if one considers just the maximum number of option. However, to quantify this distribution in space the radial distribution function (RDF) is of great practical use. It gives the probability to find a particle at a certain distance from a reference

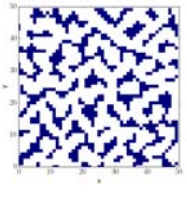

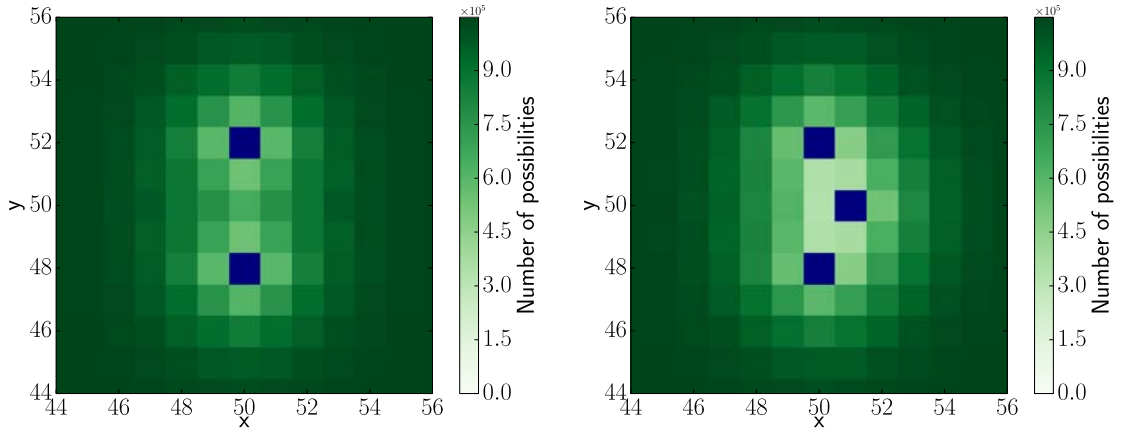

Figure 10: Examining single particle interaction: (a) Interaction of two particles in free space. In green the number of options for the particles, located at (50,48) and (50,52), are shown for time horizon $\tau = 10$. The number of options is smaller towards the other particle, therefore the particles move apart. (b) Examination of lane formation: the number of options for the particle at (51,50) is smaller towards (50,50) compared to (52,50), therefore no lanes are expected.

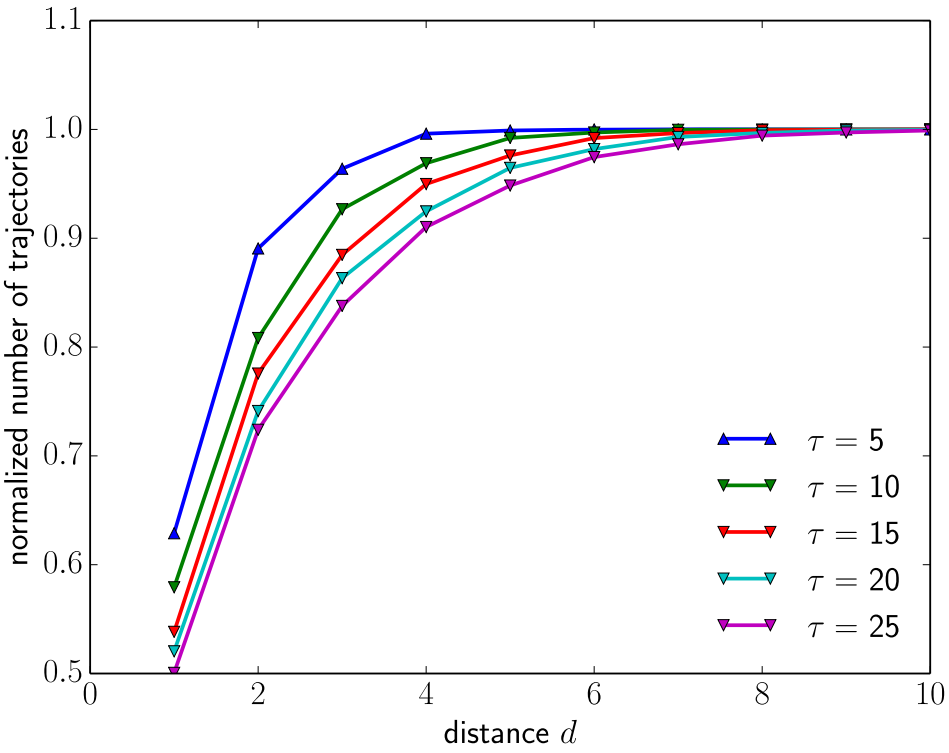

Figure 11: The phase space volume for two particles interacting at varying distances increases monotonically with distance for all τ. Hence the force is strictly repulsive.

particle

$$g(r) = \frac{V}{N^2} \left\langle \sum_i \sum_{j \neq i} \delta(\boldsymbol{r} - \boldsymbol{r}_{ij}) \right\rangle \tag{24}$$

where N is the total number of particles, V the volume (or area in 2D) available, and $\delta(\boldsymbol{r})$ is the Dirac delta distribution. The RDF is evaluated with the L_1-norm, defined as

$$|\boldsymbol{x}| = \sum_{r=1}^{n} |x_r| \ .$$

This is plausible since the particles live in a Manhattan metric and an analysis using a different metric would cause a systematic error caused by a metric transformation. In Figure 12 the RDF for $\tau \in \{15, 20\}$ and density $\rho = 0.3$ is shown. It can be seen that the particles try to keep a minimum distance of 4-5 lattice sites between each other.

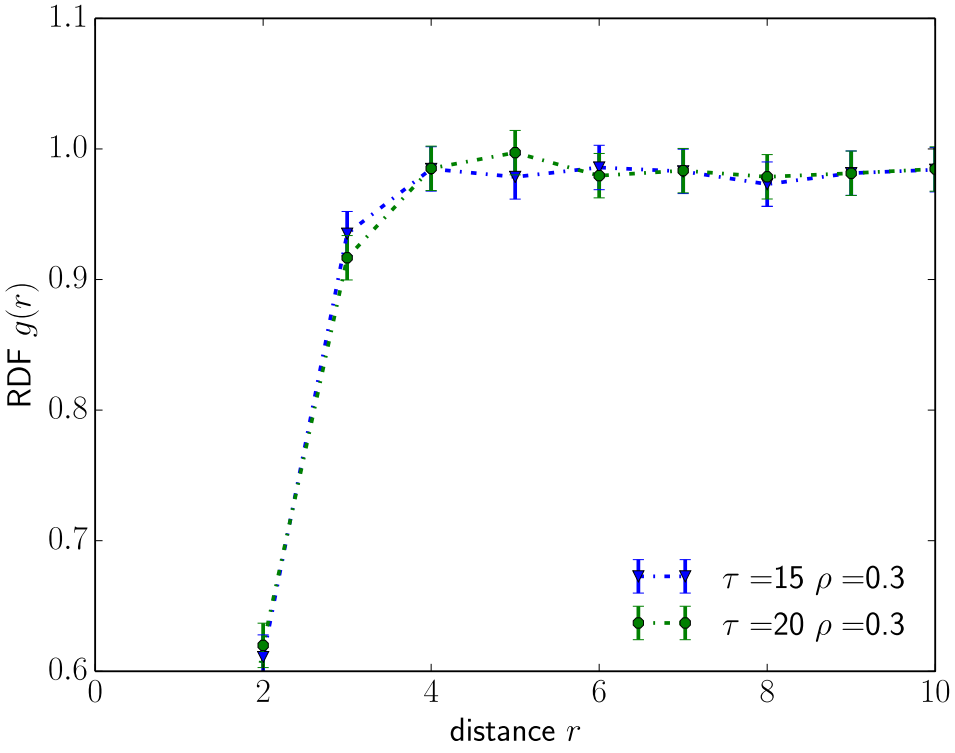

Figure 12: Average RDF over 100 timesteps after transient time $t_{\text{transient}} = 100$ in L1-metrik for different time horizon $\tau \in \{15, 20\}$ and a density of $\rho = 0.3$, shows that the particles tend to be further apart than a minimum distance. Furthermore the position of the maximum of the RDF increases with τ.

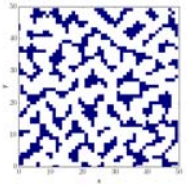

The correlation between the change of density and the shift of the first peak of the RDF is negative. This phenomena can be explained by the repulsive force of the particles. The particles try to find a configuration of maximum distance between each other. But certainly there is a defined maximum average distance since particle number conservation in a finite space does not allow infinite distances. Hence an equilibrium distance is achieved depending on particle density. To have further evidence a second neighbor peak would strengthen this argument. Indeed a second peak might be seen but is blurred due to noise and further statistics would be necessary.

The variation of τ results in a more significant first peak for a value of about $\tau = 15$. This can be understood from the fact that for smaller values of τ the trajectories are too short and approach the minimum average distance. On the other hand, a very large τ causes the trajectories to find local accumulations of particles, rather than evaluate their options just by the next and second next neighbors. This also causes the signal to become blurred. As a result we find a $\tau \approx 15$ for which the effect of the causal entropic force on structure formation is largest.

3.3 Particles in a box

For particles in a box the presence of walls does not change qualitatively the behavior of the system in the absence of confinement. The only difference is that the particles also tend to keep a distance from the walls. The particle density is therefore larger in the middle and the RDF shifts slightly, but this is within the noise level for my statistics. As an example, I show in Figure 13 a snapshot of the system after a transient time $t_{\max} = 100$.

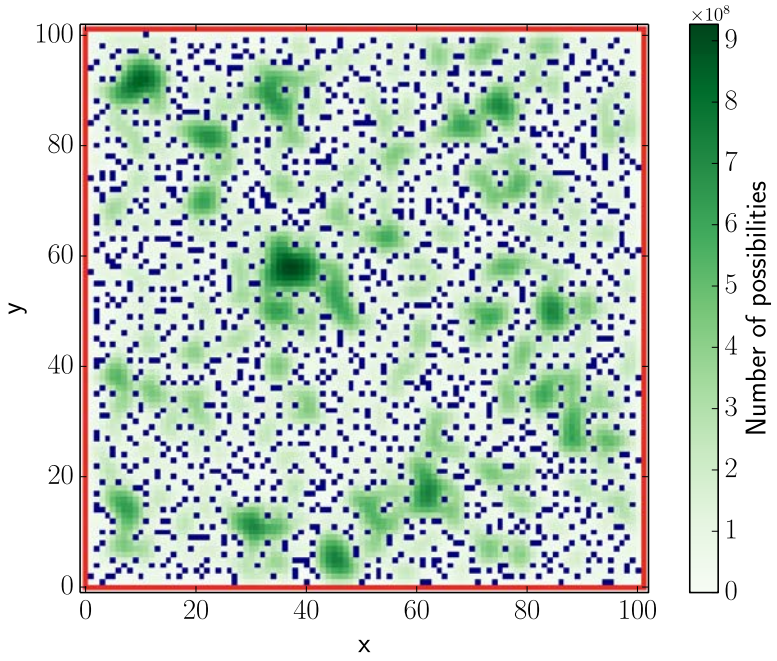

Figure 13: A snapshot of a system in a box after $t_{\max} = 100$ with $\rho = 0.15$ and $\tau = 15$. The particles behave similar to open space, where they try to maximize the distance to all other particles, moreover they keep some distance from the walls.

3.4 Bottleneck

The bottleneck problem is an elegant way to simulate evacuation scenarios. For pattern forming particles it was found by Hornischer that lanes form. Using approach A described above I find that the particles escape from the bottle due to entropic pressure. The rate of escaped particles depends on the bottle's size: if the space within the bottle is bigger there are more possibilities to move within the bottle and therefore relatively less attraction from the possibilities outside.

The same applies for a smaller external box, namely fewer possibilities outside cause less attraction. Hence, the number of escaping particles depend on the ratio of the bottle's size and the outside box's size. Another dependency of the escape number is the neck's length. As the necks grow in length the number of escaping particles increases. And finally the time horizon τ: for smaller τ the particles do not see the possibilities outside the bottle and thus behave like in a box. With increasing τ the particle see the possibilities outside and the escape number increases.

Snapshots of a typical evolution for $\tau = 15$, particle number $N = 10$, bottlesize of 5, bottleneck's width $w = 1$ and box's size of 50 are shown in Figure 14. It also shows also that there is always only one particle in the bottleneck, since the bottleneck is clogged for the sampling trajectories when one particle is in the bottleneck.

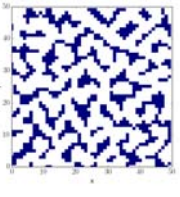

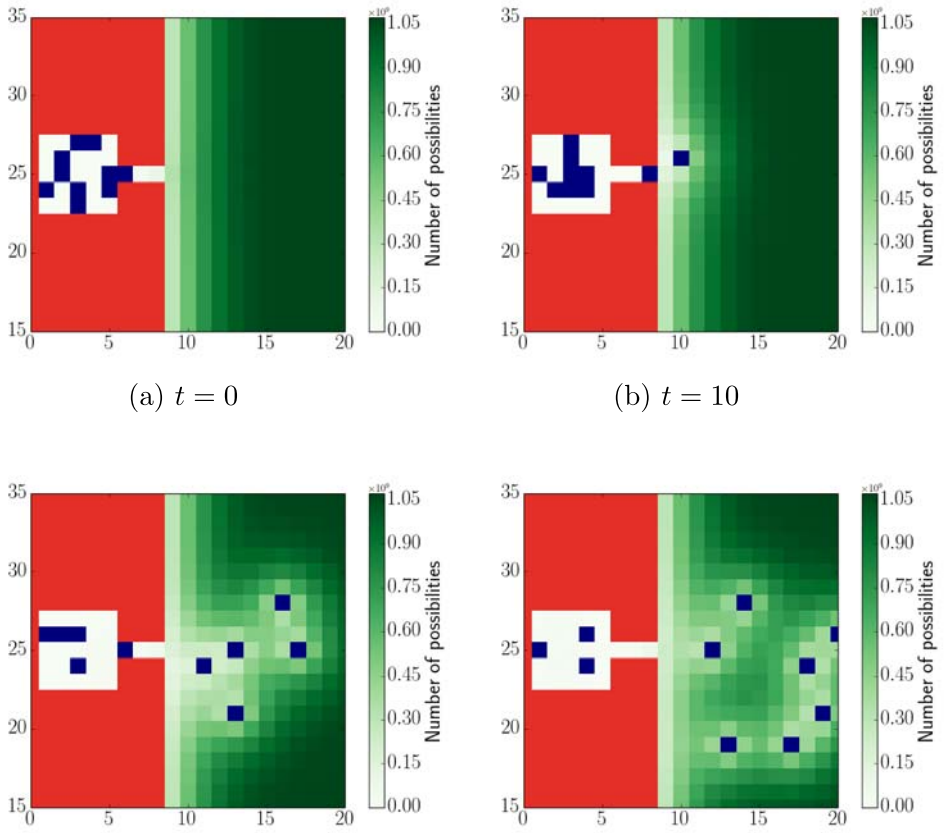

(a) $t = 0$ (b) $t = 10$

(c) $t = 50$ (d) $t = 150$

Figure 14: A typical evolution of escaping particles in a bottleneck with 10 particles, $\tau = 15$ and a necklength of $l = 3$. Shown are snapshots of the random starting condition, after 10, 50 and 150 timesteps, respectively.

The dependencies on τ and the neck's length l are further evaluated in Figure 15. It shows an average over 10 runs of the number of particles escaped from the bottle after $t_{\max} = 200$. The number of escaped particles increases with decreasing l and increases with τ. To put this number of escaped particles into perspective Figure 16 shows the number of escaped particles which perform a random walk in the same color code. This number is 5.2 for a neck's length of $l = 1$ and decreases monotonically to 1.4 for $l = 10$. Comparing the random walk particles now with the particles under the influence of causal entropic force it shows that the former perform better for all $\tau \in \{5, 20\}$ compared to the latter.

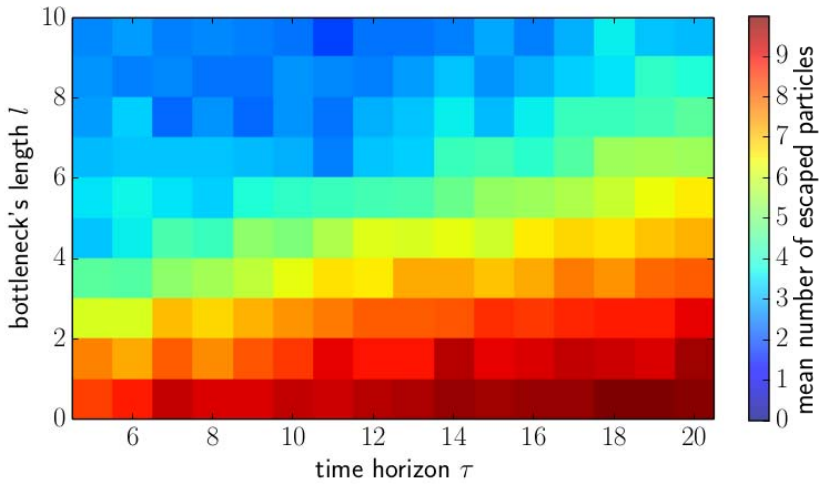

Figure 15: The phase-space of number of escaped particles through a bottleneck with width $w = 1$ after $t_{\max} = 200$ averaged over 10 runs shows a positive dependency with τ and a negative with l. For all τ the number of escapes particles is higher compared to random walk particles of Figure 16.

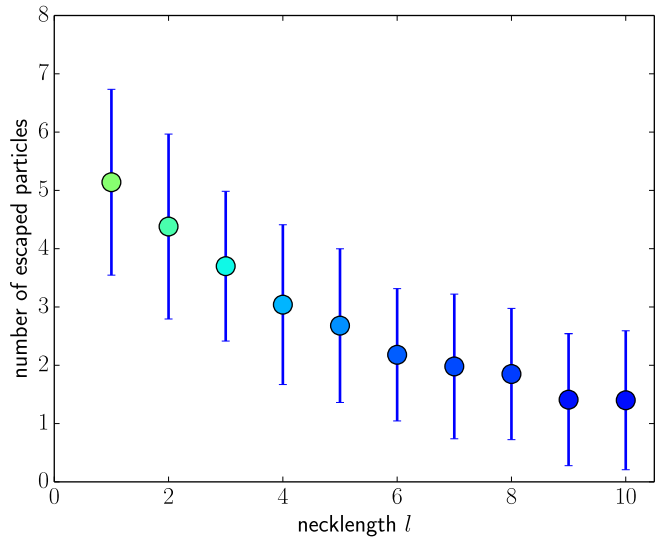

Figure 16: Number of particles escaped through a bottleneck with random walks after $t_{\max} = 200$ with a bottle's size of 5 and a neck's width $w = 1$.

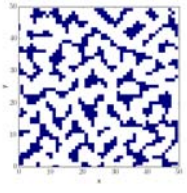

4 Approach B and C: Causal entropic force

In this section I present the results of a single particle interacting with a wall in section 4.1 and with another particle in section 4.2. I explain my findings in free space for approach B in section 4.3.1 and C in section 4.3.2. I then introduce noise as an attempt to find global minima rather than very local ones in section 4.4. And finally in section 4.5.1 return to the bottleneck for approach B and in section 4.5.2 for approach C.

4.1 Particle wall interaction

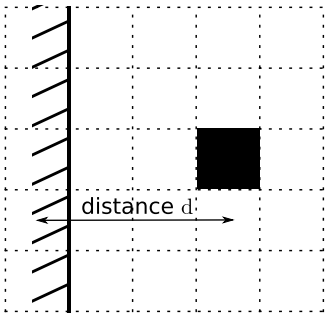

Figure 17: Interaction of a particle with a wall at distance d.

The interaction of a particle with a hard wall is the strongest constraint of phase space to one side, compared to no obstacles to the other side this results in the highest gradient of restriction. Among all trajectories that would be possible in free space are excluded those which cross lattice sites in the restricted area (see Figure 17). Then, the average is taken over the remaining sampling trajectories. Figure 18 shows the dependence of the normalized phase space volume on distance from the wall for $\tau = 5, 10, 15, 20, 25$ for approach B, and Figure 19 for approach C. If the horizon τ is smaller than the distance from the wall no interaction is observed. For small $\tau < 3$ (approach B) and $\tau < 4$ (approach C) a monotone increase of the phase space volume is observed with increasing distance to the wall, hence the absolute minimum is at distance 1. For larger τ the minimum shifts to larger values and hence the phase space volume of distance 1 is higher than distance 2. This means the particle rather wants to be right next to a wall than at a small distance. The dependence of the minimum with τ is positive for both approaches B and C, but the rate is higher for the approach A, as shown in Figure 23. Comparing the absolute value of the phase space volume of the position right next to the wall (distance $d = 1$) with the limit of large distances reveals that the distance $d = 1$ becomes increasingly favourable with increasing τ and exceeds the value for the phase space volume of the particle at large distances for $\tau = 9$ and $\tau = 26$, respectively.

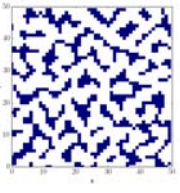

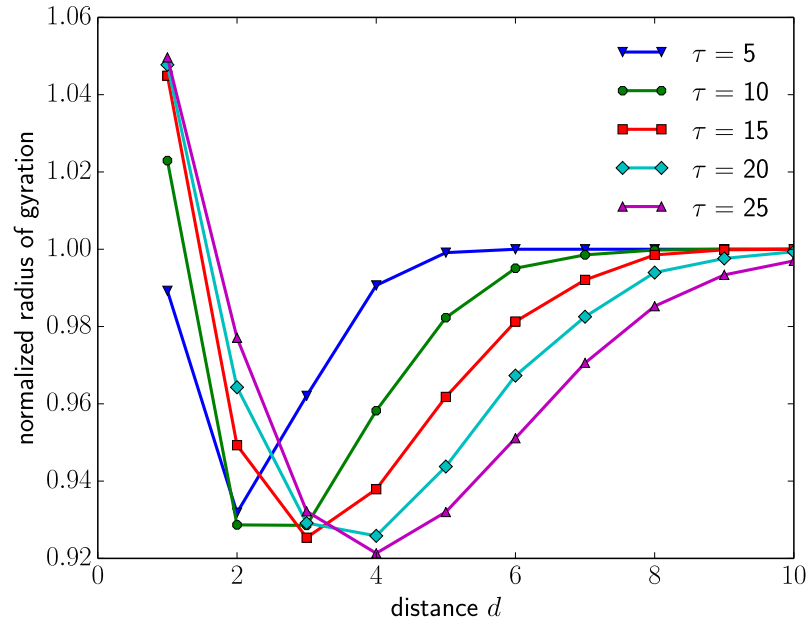

Figure 18: Particle wall interaction for different distances from the wall has a minimum whose position increases with τ. Hence the particle favors to be right next to the wall or far away from it rather than at medium distances. Here the position with distance $d = 1$ is favorable for $\tau < 9$ compared to the limit of large distances.

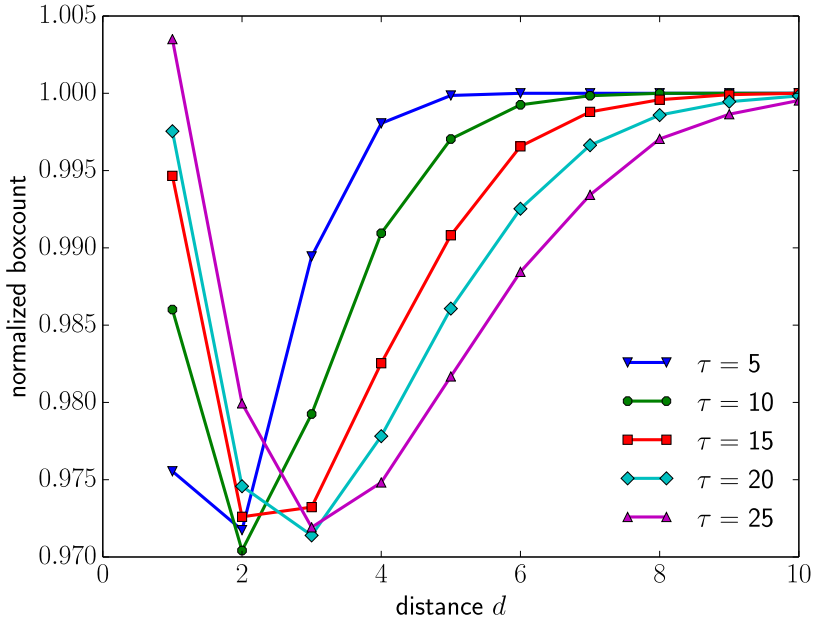

Figure 19: Particle wall interaction for different distances from the wall has a minimum whose position increases with τ. Hence the particle favors to be right next to the wall or far away from it rather than at small distances. For approach C the position with distance $d = 1$ is favorable for $\tau < 26$ compared to the limit of large distances.

4.2 Particle particle interaction

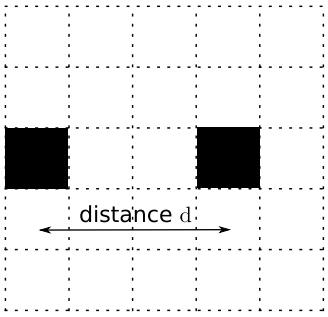

Figure 20: Interaction of two particles at distance d.

After having found complex behavior for the particle wall interaction, I turn to the interaction of two particles separated by a distance d and with this I lay the basis for studying many particle systems (see Figure 20). In Figure 21 the normalized phase space volume is shown with respect to the distance of the two particles d for $\tau \in \{5, 10, 15, 20, 25\}$ for approach B and in Figure 22 for approach C. It shows that for $\tau < 3$ (approach B) and $\tau < 4$ (approach C) a monotone increase with increasing distance d of phase space volume is observed. For larger τ the position of the minimum of the phase space volume increases to larger d, which is shown in Figure 23.

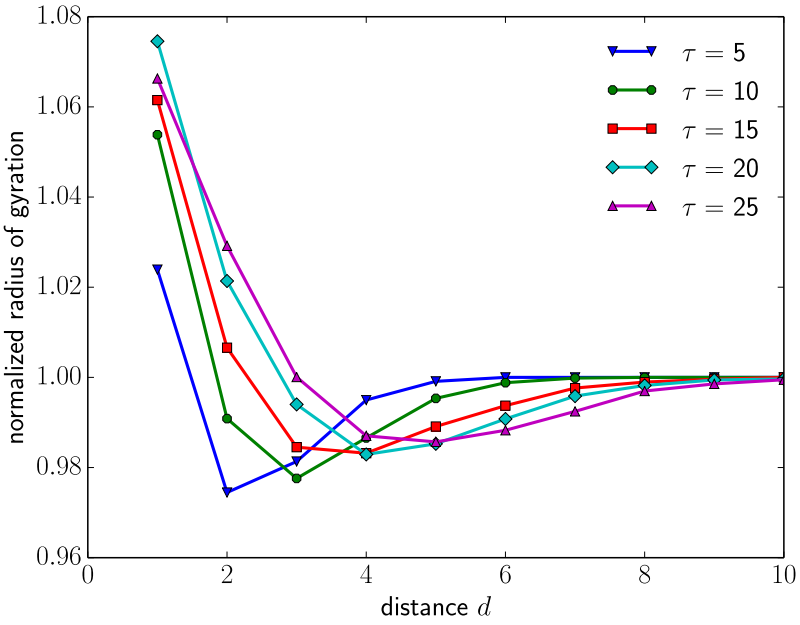

Figure 21: The radius of gyration of a particle interacting with another particle has a minimum whose position increases with τ. The position right next to a particle is more favorable compared to the limit of large distances for all τ.

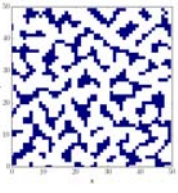

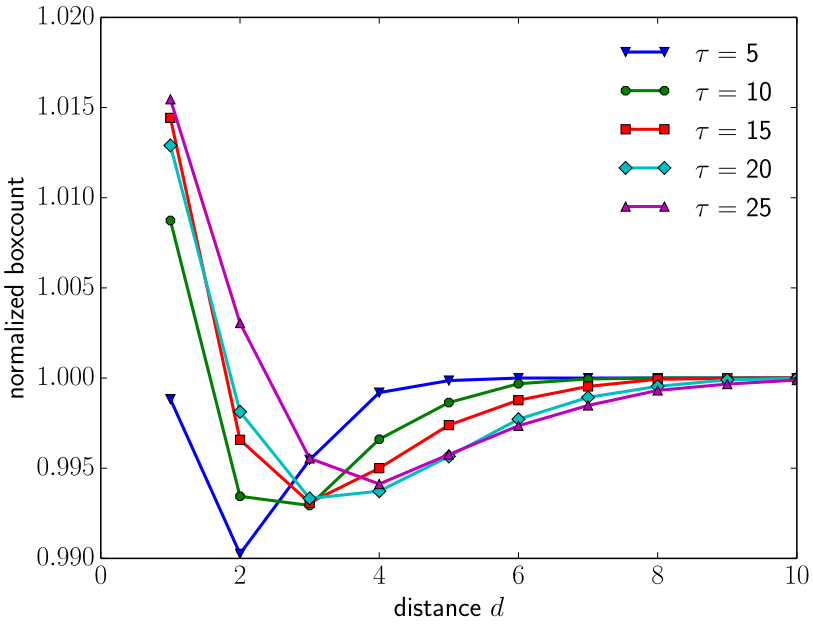

Figure 22: The boxcount of a particle interacting with another particle has a minimum whose position increases with τ. The position right next to a particle is more favorable compared to the limit of large distances for $\tau > 7$.

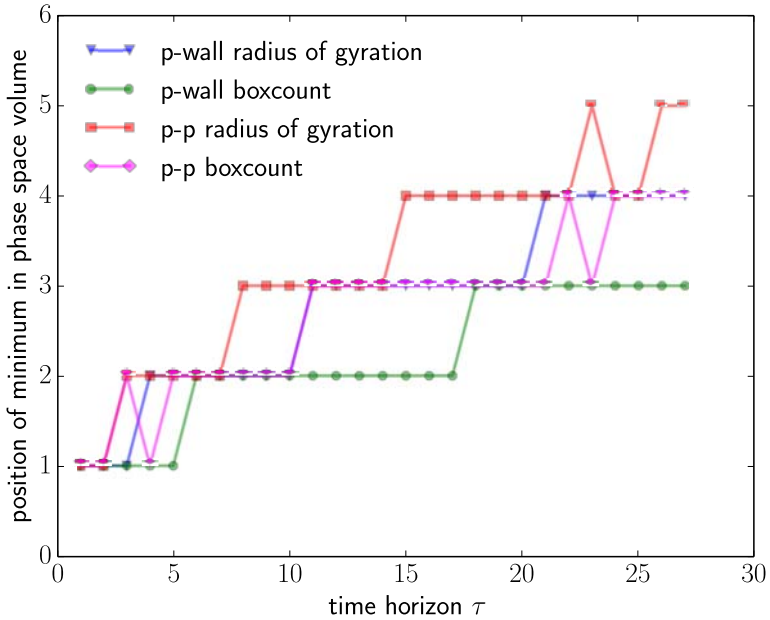

Figure 23: Position of the phase space volume's minima for varying τ for the particle-wall interaction and the particle-particle interaction for both approaches B and C. It shows an increase with respect to τ. The method B has a higher increase with τ compared to method C. And the increase of the position of the minimum for particle-particle interaction is faster compared to particle wall interaction for both B and C.

Hence particle-particle interaction shows similar behavior to the findings of particle-wall interaction of the previous section 4.1. All examined interactions show an increase of the phase space volume minima's position with time horizon τ. The dependency for approach B is in both cases stronger compared to approach C.

4.3 Free space

In this subsection I describe the algorithmic structure for approach B and C before discussing the results of approach B and C individually, to then compare them.

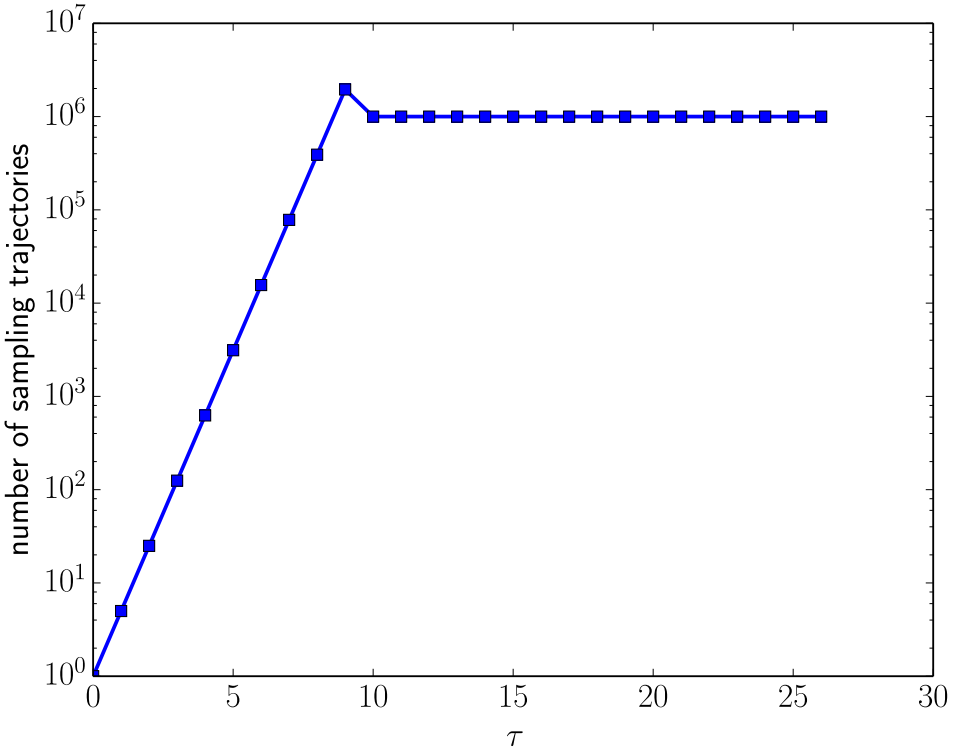

Figure 24: Number of sampling trajectories $s_{\max}$ with respect to τ increases exponentially until computational costs need it to be limited to a fixed number s_{cutoff}

Algorithmic structure The algorithm considers at first one particle in free space without any obstacles. Here the number of possible sampling trajectories grows as 5^τ. Since this exponential growths of sampling trajectory numbers runs into computational problems at some point, I used a cutoff in the number of sampling trajectories I consider. For $5^\tau = s_{\max}(\tau) < s_{\text{cutoff}}$ I calculate all sampling trajectories, for those τ larger than τ_{cutoff} I pick a random ensemble of different sampling trajectories with size s_{cutoff}. Hence not the whole phase space is explored for large τ. For approach B I use throughout all simulations a $s_{\text{cutoff}} = 10^5$; for approach C, I use

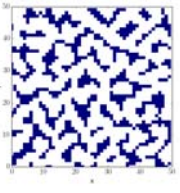

$s_{\text{cutoff}} = 10^5$ if not stated otherwise, and $s_{\text{cutoff}} = 10^6$ in some explicitly mentioned cases. With these sampling trajectories I generate a map which gives me all sampling trajectories for a given lattice site which cross this lattice site. I also compute for every sampling trajectory the phase space volume, i.e. the radius of gyration or the boxcount. These data are stored and used for all simulations with a given τ. The actual simulation does not need to generate sampling trajectories, but uses the map with relative coordinates for all particles and all obstacles in range of τ to identify those sampling trajectories, which need to be excluded, because they are not realizable for the current state. It generates a Boolean array with $True$ for all realizable trajectories and $False$ for non-realizable ones and uses this as a mask to calculate the mean over all remaining sampling trajectories for each first step. As a result I obtain five numbers, which correspond to the average phase space volume for sampling trajectories starting from the four neighboring lattice sites and the site of the particle. This is done for all particles and then all particles are moved in random order. If the lattice site with the highest phase space volume for one particle is already occupied, since another particle already moved there, the particle does not move for this timestep.

4.3.1 Approach B

The simulations for approach B evolve from random initial conditions towards a steady-state in less than 30 time steps. A typical evolution of a system for $\tau = 15$ and $\rho = 0.35$ is shown as an animation of figures in the bottom right corner of every odd page when rapidly turning the pages of this thesis and using it as a flipbook. The patterns, which can be observed, are different in size and appearance for different time horizon τ and density ρ. Typical steady-states for $\tau \in \{5, 10, 15, 20, 25\}$ are shown for different densities $\rho \in \{0.25, 0.3, 0.35\}$ in Figure 25. It shows that labyrinthine patterns form for $\tau = 5$ for all densities $\rho \in \{0.05, 0.1, 0.15, 0.2, 0.25, 0.3, 0.35, 0.4, 0.45, 0.5\}$ and for $\tau = 10$ the density has an influence on the appearance of the patterns: for low densities $\rho < 0.3$ labyrinthine patterns form, however for $\rho \geq 0.3$ the patterns gradually form barriers in the labyrinth and move towards a pattern with hexagons, pentagons and tetragons. With increasing τ the tubes as well as the polygons increase in width.

To quantitatively characterize the different appearances of the steady-states I use the radial distribution function, which is a measure for the average distance between the particles and given in Eq. (24). Figure 26 shows the RDF for $\tau = 10$ and $\rho = 0.25$. The first value at $r = 1$ is correlated to the first neighbor particles within one cluster. The first peak is due to the distance d between the patterns, as shown in Figure 27. Also the second peak is due to twice the distance of the

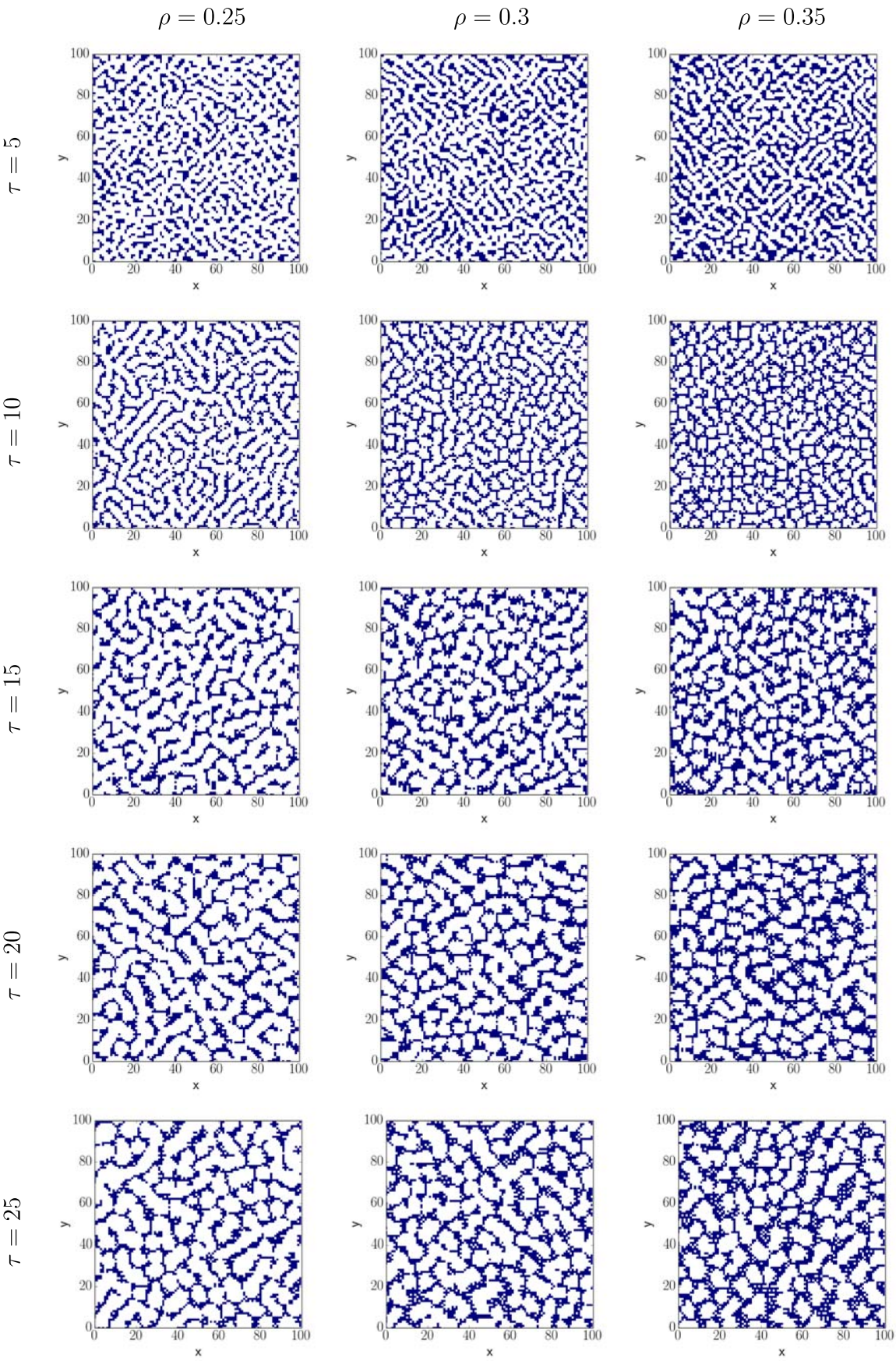

Figure 25: Steady-state for $\tau \in \{5, 10, 15, 20, 25\}$ and particle number $\rho \in \{0.25, 0.3, 0.35\}$.

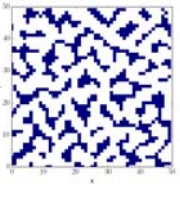

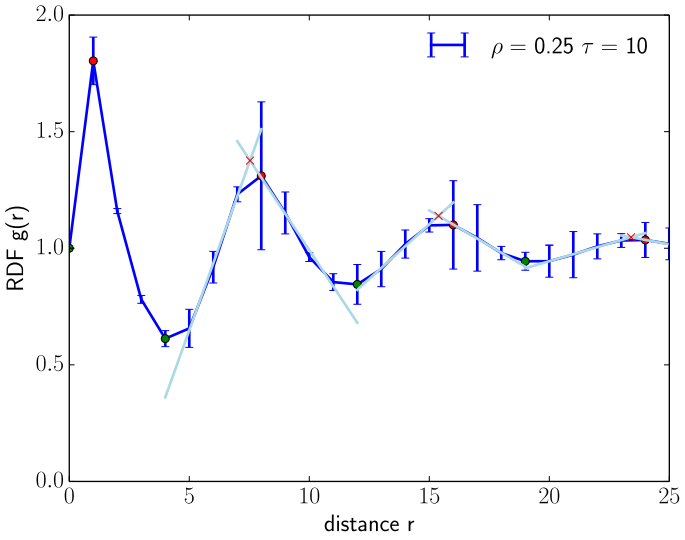

Figure 26: The RDF shows a high starting value at distance $r = 1$ the first peak at $r = 8$ or with triangulation of the peak's flank at $r = 7.4$. The following peak is a second neighbor peak at $r = 15$ (for triangulation $r = 15.4$). Even peaks of higher order can be observed.

patterns. The position of the RDF-peak is marked with the red dot on the RDF function. However to gather more information I used two flanks on both sides of the peak constructed by a linear fit through the data between minimum and maximum. The position of their intersection traces a continuous locus. This however fails for the starting value because there are no points to construct a flank lower than the $r = 1$, but works for all other peaks.

To further explore the appearance of the patterns Figure 28 shows the position of the first, second and third RDF peak in dependence of a varying $\tau \in [5, 27]$. The high value for the RDF at $r = 1$ occures for all simulations and is therefore not shown here. It shows that the distance between the particles increases with τ. A linear fit of the peak's position gives a slope for the first peak of $m_{1\text{st}} = 0.27$ with a correlation coefficient of $r_{1\text{st}} = 0.996$. For the fit of the higher order peaks the value of the slope almost doubles to $m_{2\text{nd}} = 0.51$ for the second order and remains at $m_{3\text{rd}} = 0.54$ for the third order. The correlation coefficient decreases slightly to $r_{2\text{nd}} = 0.98$ and $r_{3\text{rd}} = 0.95$. The doubling of the slope for first and second order peak shows that locally there is order, as in a crystal. However, the third peak shows almost the same slope and hence globally there is disorder, not at all behaving like a crystal. Finally it shows that the value for $\tau = 10$ is significantly lower compared to the linear fit.

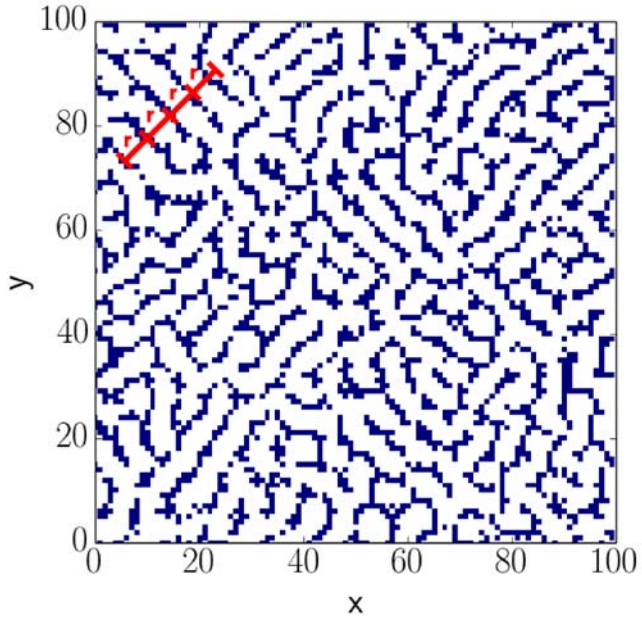

Figure 27: The steady-state (reached after t = 17) of a simulation with $\tau = 10$, $\rho = 0.25$. The peaks of the RDF can be observed as the typical length scale of the distance between two particles. Where one red marker indicates the length of $r = 7.3$, which is the first peak of the RDF in Figure 26.

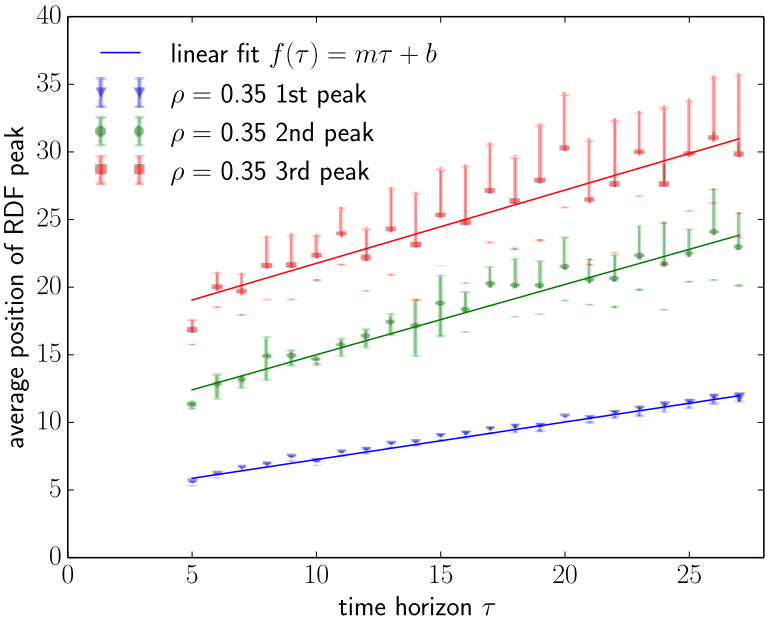

Figure 28: Dependence of average RDF peak's position over 10 simulations of $\rho = 0.3$ with respect to τ is positive. A linear fit matches the data with an correlation coefficient of $r_{1st} = 0.996$, $r_{2nd} = 0.98$, $r_{3rd} = 0.95$ for the first, second and third peaks, respectively. The slope of the line is for the first peak $m_{1st} = 0.27$, for the second $m_{2nd} = 0.51$ and for the third peak $m_{3rd} = 0.54$.

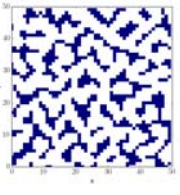

The independence of the position of the RDF peak with respect to the density is supported by Figure 29, which shows that the peak positions are independent of the density for $\tau \in \{5, 15, 20, 25\}$ and negatively correlated for $\tau = 10$. The negative correlation can be understood by the change in methodology, where only a fraction of the phase space is explored with sampling trajectories, hence the clusters are more noisy and smaller. Small clusters however are effected more by an increase in density and then stuck closer together, due to particle pressure. The error bars of the second neighbor peaks in Figure 28 as well as in Figure 29 are larger since the signal is more blurred. Also the error bars increase for very high and low densities, since patterns are less prominent for these range of densities and the RDF peak's positions have a larger variance.

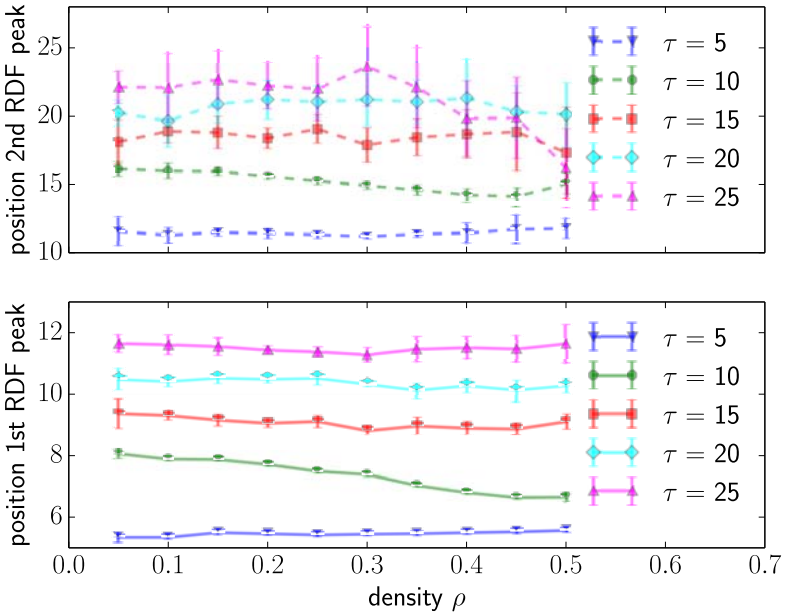

Figure 29: Average of RDF peaks of the steady-state of 10 different initial positions for $\tau \in \{5, 10, 15, 20, 25\}$ and density $\rho \in \{0.05, 0.1, 0.15, 0.2, 0.25, 0.3, 0.35, 0.4, 0.45, 0.5\}$. The position of the RDF peaks are independent of the density for all τ, except $\tau = 10$ where the dependence is negative. Positive dependence of τ can be seen as Figure 28 illustrates.

To quantify the appearance of the patterns I introduce two new observables: the cluster and the void numbers. A cluster is a local interconnected region of particles and a void is an interconnected region, where no particles are. Labyrinthine patterns do have a finite number of clusters, depending on the density and a very small if not only one void. Noisy configurations have a number of clusters of the order of particle number and a void number close to one. Polygonal patterns have a finite number of clusters, also depending on the density, but a higher number of voids. I define

the intersection of cluster number and void number as the point of phase transition between labyrinthine and polygonal phases for non-noisy states. This corresponds to the zero of the Euler characteristic, which can be defined as the difference of the number of clusters and the number of voids [19]. Figure 30 shows that the number of clusters increases with density until a maximum is reached and a further increase in density only results in an increase of the cluster size but not in the number. For all $\tau \in \{5, 10, 15, 20, 25\}$ the void number starts to increases for $\rho \approx 0.3$. All values of the density for the maximum cluster number decrease for increasing τ except the one for $\tau = 10$, which shows an abrupt increase compared to the curves of $\tau = 5$ and $\tau = 15$. This fact supports the statement that the patterns are more noisy for $\tau = 10$ due to the change of methodology of algorithm. The intersection of cluster and void number is given in Table 1. The phase transition from labyrinthine to polygonal patterns hence occurs for increasing τ with decreasing density ρ. Figure 32 shows the transition for an average over 4 runs for each point in $\tau \in [5, 25]$ and $\rho \in [0.05, 0.5]$. The line of phase transition does show a decrease in slope for increasing τ, which seems to converge towards a value of $\rho \approx \frac{1}{3}$. The transition is therefore far off the percolation transition for random processes, which is at a density of $\rho = 0.592$ on the square lattice [20].

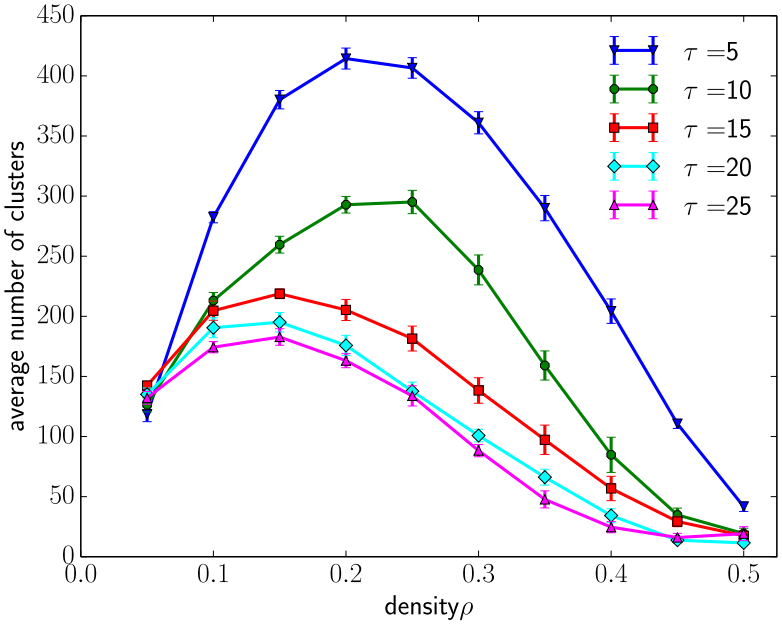

Figure 30: Number of clusters of particles increasing with density and saturates where the cluster's size increases and cluster interconnect.

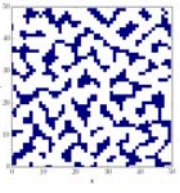

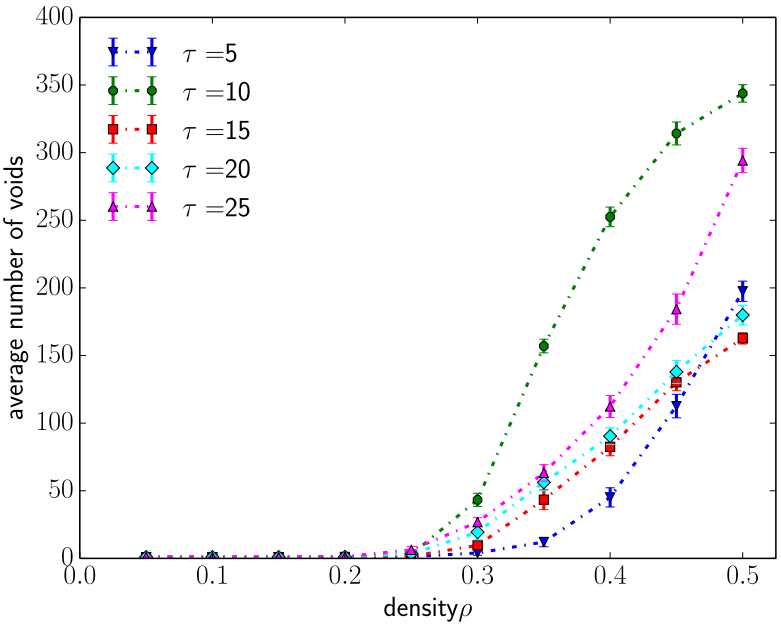

Figure 31: The number of voids is around 1 for low density and indicates the formation of cells from a density of $\rho = 0.3$.

τ	5	10	15	20	25
Intersection	$\rho = 0.45$	noisy	$\rho = 0.39$	$\rho = 0.36$	$\rho = 0.34$

.

Table 1: The phase transition from labyrinthine to polygonal patterns occur at decreasing density ρ for increasing τ

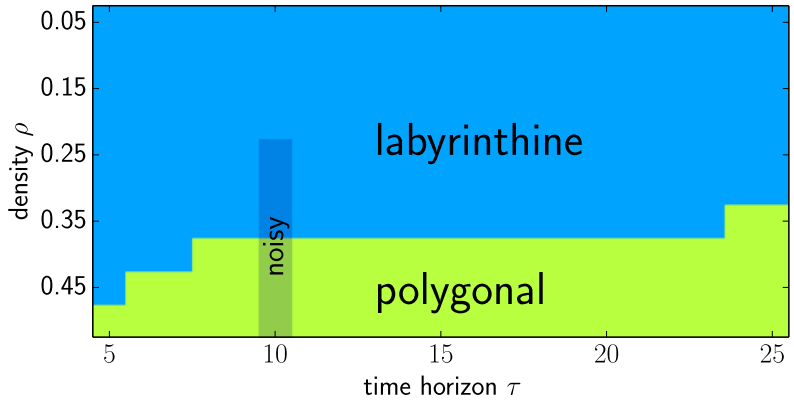

Figure 32: Phasespace of pattern for $\tau \in [5, 25]$ and $\rho \in [0.05, 0.5]$ shows transition from labyrinthine pattern (number of clusters>number of voids) to polygonal pattern (number of clusters<number of voids) for increasing τ and ρ. Each data point is the average over 4 runs.

4.3.2 Approach C

After examining approach B to quantify the phase space volume in Eq. (12), I turn again to approach C introduced in section 2.1.5. The configurations of the particles after $t_{\max} = 50$ for $\tau \in \{5, 10, 15, 20, 25\}$ and density $\rho \in \{0.15, 0.3, 0.45\}$ are shown in Figure 33. For $\tau = 5$ this state is a steady-state and no movement except a small jitter occurs. For $\tau \geq 10$ there is still movement and no steady state is reached within time $t_{\max} < 200$, which was the maximum time I considered. For the runs of $\tau \in [10, 15]$ the particles still move a lot, but for $\tau > 15$ the movement of the particles is lower and only small fluctuations are observed.

The appearance of the pattern differs from the patterns of approach B. For $\tau = 5$ it shows more rectangular patterns with smaller clusters of particles. For $\tau = 10$ the patterns disappear for $\rho > 0.2$ and the signal is very blurred and noisy, this is still true for $\tau = 15$ even though one can start to see the reappearance of patterns. For $\tau > 15$ the patterns reappear with a different morphology. The patterns are now labyrinthine for densities $\rho \leq 0.25$ and polygonal for $\rho \geq 0.3$. The clusters of high density and large τ show that the position $r = 2$ become more likely. This can also be seen in the RDF distribution in Figure 34, where $g(r = 2)$ is larger than $g(r = 1)$, whereas for simulations with $\tau < 10$ this difference is in the order of $g(r = 1) - g(r = 2) \approx 0.3$. This can be understood by inspecting Figure 22: it shows that the minimum of the phase space volume increases with τ and the difference between $\Omega(r = 1)$ and $\Omega(r = 2)$ decreases with τ, hence the likelihood of finding a particle for $r = 2$ increases with τ.

Quantifying dependencies of the pattern structure with respect to τ and ρ leads us again to the RDF, whose first, second and third peak are shown in Figure 35 for varying τ. The patterns form and the peak's position increases linearly with τ until $\tau = 10$. For $\tau \in [10, 15]$ the pattern breaks down and the peak's position is noisy and drops down from the linear increase. For $\tau \geq 16$ the patterns reappear and the peak's positions are increasing linear again matching the line of the fit for the peak's position for $\tau < 10$. The slope of the fit excluding the range of $\tau \in [10, 15]$ for the first order is $m_{1\text{st}} = 0.24$ with a correlation coefficient of $r_{1\text{st}} = 0.99$, for the second order peak the slope doubles as also observed for approach B to $m_{2\text{nd}} = 0.50$ with $r_{2\text{nd}} = 0.99$, hence locally shows order. The slope of the third peak is $m_{3\text{rd}} = 0.66$ with $r_{3\text{rd}} = 0.96$, which does still show an increase but is not three times the slope of the first order. Hence the approach C shows order in a wider range compared to approach B.

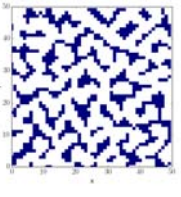

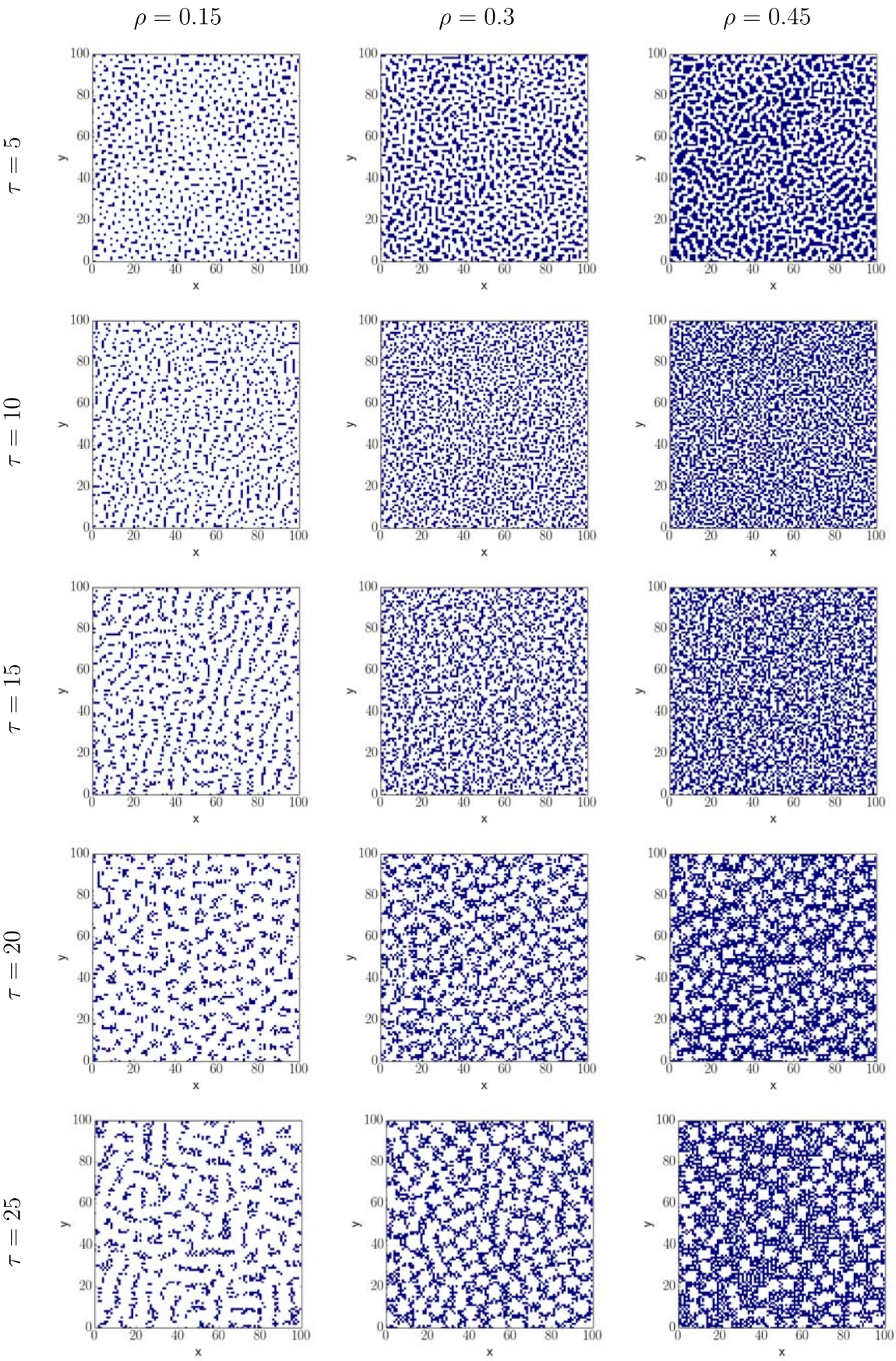

Figure 33: Steady-state for $\tau \in \{5, 10, 15, 20, 25\}$ and density $\rho \in \{0.15, 0.3, 0.45\}$.

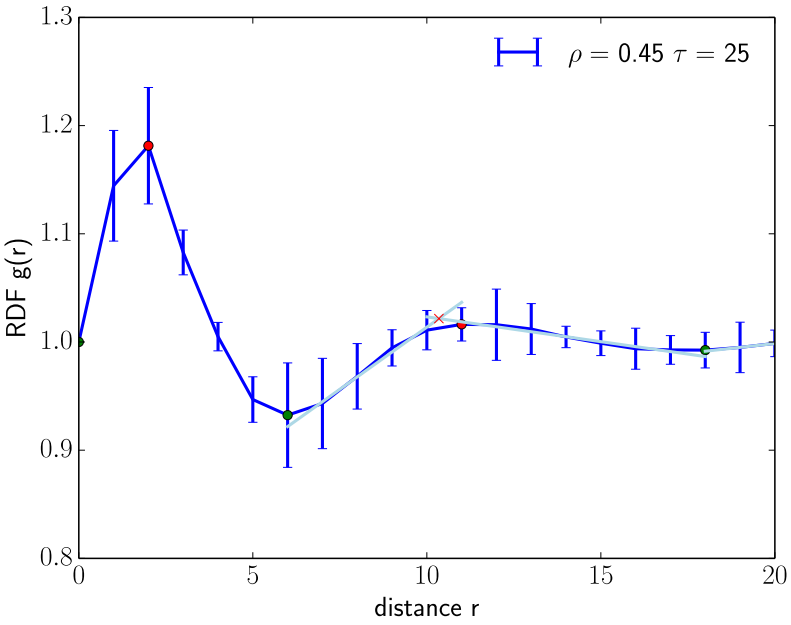

Figure 34: RDF for $\tau = 25$ and $\rho = 0.45$ shows that g(r=1) is smaller compared to g(r=2).

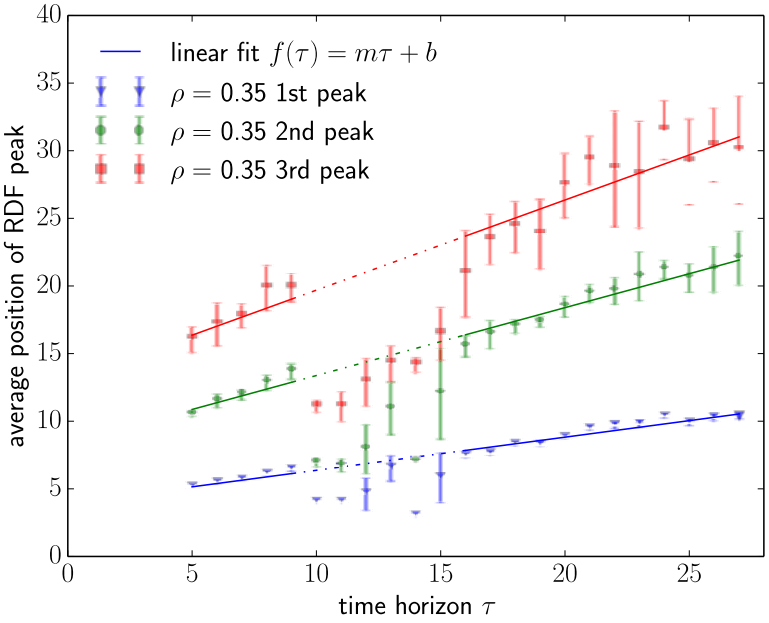

Figure 35: Dependence of average RDF peak's position over 10 simulations with respect to τ is positive. A linear fit matches the data excluded the noisy region of $\tau \in [10, 15]$ with an correlation coefficient of $r_{1\text{st}} = 0.99$, $r_{2\text{nd}} = 0.99$, $r_{3\text{rd}} = 0.96$ for the first, second and third peaks, respectively. The slope of the line is for the first peak $m_{1\text{st}} = 0.24$, for the second $m_{2\text{nd}} = 0.50$ and for the third peak $m_{3\text{rd}} = 0.66$.

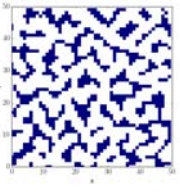

The dependence the RDF peaks' position with respect to the density ρ is shown in Figure 36. Here it shows that the RDF peak is uncorrelated to density for $\tau \in \{5, 20, 25\}$. For $\tau \in \{10, 15\}$, where the noisy patterns were found it shows that the peak shows a realtive constant value for $\rho < 0.25$ before the peak's position drops abruptly. Also by looking at the steady states it shows that for $\rho < 0.25$ patterns occur. Hence I can conclude that only for the range of values $\tau \in [10, 15]$ and $\rho \geq 0.25$ the patterns do not occur.

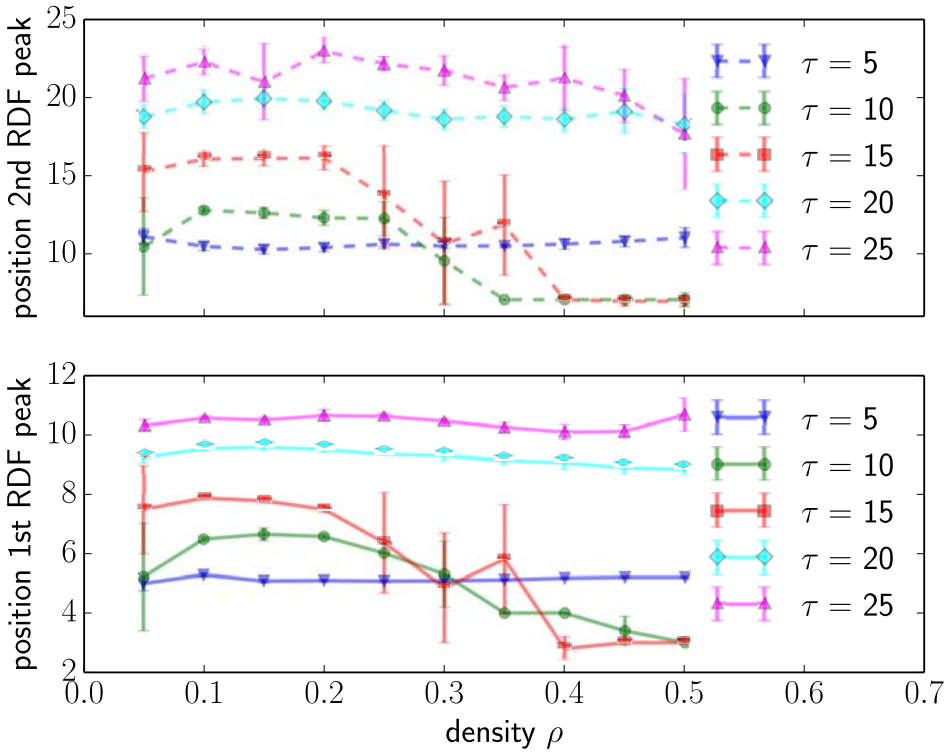

Figure 36: Dependence of RDF peak for varying $\rho \in [0.05, 0.5]$ for $\tau \in \{5, 10, 15, 20, 25\}$. It shows that for $\tau \in \{5, 20, 25\}$ the peak-density dependence is constant. For $\tau \in \{10, 15\}$ the peak's position is first increasing, then constant and for $0.25 \leq \rho < 0.4$ the peak's position drops with high variance, and for $\rho \geq 0.4$ another tableau is reached, where the second peak's position matches the constant value of the first peak's position for small ρ.

Looking at the cluster and void numbers reveals that for $\tau \in \{10, 15\}$ the cluster number is considerably larger than the cluster number for $\tau = 5$, which is another confirmation of the noisy appearance of the particles for $\tau \in [10, 15]$ and $\rho \geq 0.25$. For the other values of $\tau \in \{5, 15, 20\}$ the intersection between cluster number and void number is given in Table 2, which shows a negative correlation of τ and ρ for the phase transition. In Figure 39 the phase space for $\tau \in [5, 25]$ and $\rho \in [0.05, 0.5]$ is displayed and reveals a smooth line of phase transition for varying τ with respect

to ρ. The range of values for which polygonal patterns appear is smaller compared to approach B which can be understood by weaker weight of approach B compared to approach C examined in Figure 5, but again I can conclude that the transition is far off the percolation transition for random processes $\rho = 0.592$.

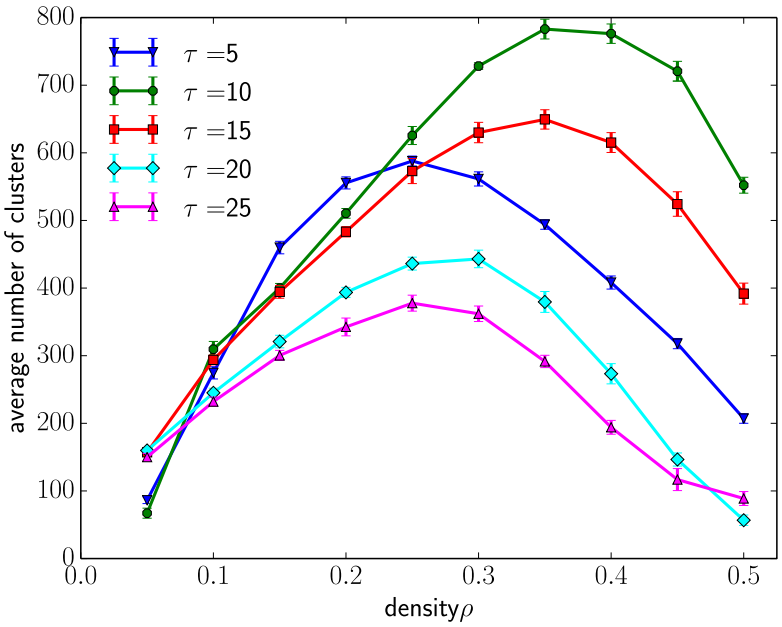

Figure 37: Number of clusters increases with density and saturates where the cluster's size increases and cluster interconnect for $\tau \in \{5, 20, 25\}$. For the noisy range of $\tau \in \{10, 15\}$ and $\rho > 0.25$ the number of clusters increases well above the $\tau = 5$ value of small scale patterns, which indicated very small and hence noisy appearance.

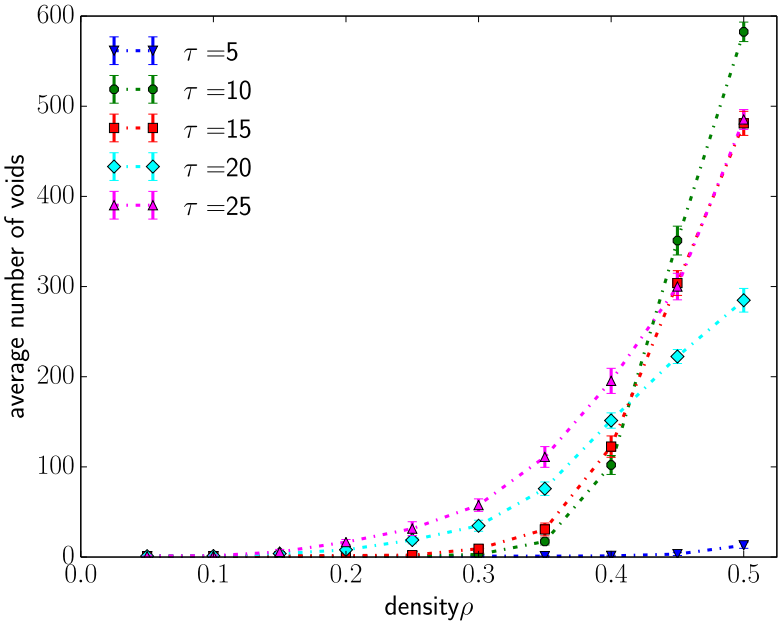

Figure 38: The number of voids is around 1 for low density and indicates the formation of cells from a density of $\rho = 0.3$, because of its increase.

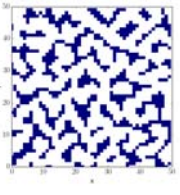

τ	5	10	15	20	25
Intersection	ρ >0.5	noisy	noisy	$\rho = 0.43$	$\rho = 0.40$

Table 2: The phase transitionoccurs for increasing τ with decreasing ρ.

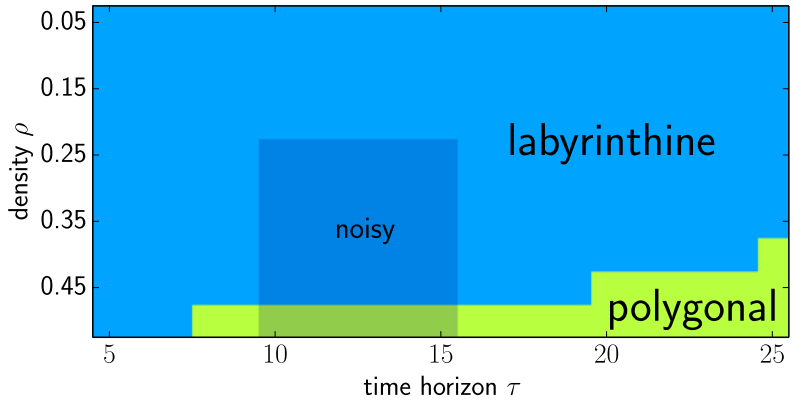

Figure 39: Phasespace of pattern for $\tau \in [5, 25]$ and $\rho \in [0.05, 0.5]$ shows transition from labyrinthine pattern (number of clusters>number of voids) to polygonal pattern (number of clusters<number of voids) for increasing τ and ρ. Each data point is the average over 4 runs.

To understand the change in behavior for $\tau \in [10, 15]$ and $\rho \geq 0.25$ one has to know, that for $\tau < 10$ I consider all possible sampling trajectories, whereas for $\tau \geq 10$ I only consider a constant number of sampling trajectories $s_{\text{cutoff}} = 10^5$, which are randomly chosen, but equally distributed in all five directions. To evaluate if the disappearance of the pattern for $\tau \geq 10$ is a feature of the method or a real phase transition at $\tau = 10$, I considered a set of simulations for $s_{\text{cutoff}} = 10^6$ and also ran simulations for $\tau = 9$ of reduced $s_{\text{cutoff}} = 10^5$ instead of $s_{\text{max}} = 5^9 = 1953125$. Figure 40 shows the position of the RDF peaks for $s_{\text{cutoff}} = 10^6$ and it shows that there is no significant difference to $s_{\text{cutoff}} = 10^5$ of Figure 35. Figure 41 shows the steady-state for $\tau = 9$ considering all sampling trajectories $s_{\text{max}} = 5^9$ and the final state after $t_{\text{max}} = 200$, which is still underlying motion for a reduced number of sampling trajectories $s_{\text{cutoff}} = 10^5$. This proves that the pattern formation disappears, when only parts of the phase space is explored and it is not a phase transition for $\tau = 10$. The part which needs to be explored however needs to be a considerable percentage of the whole phase space, since an increase from $s_{\text{cutoff}} = 10^5$ to $s_{\text{cutoff}} = 10^6$ did not cause the patterns to reappear in the range of $\tau \in [10, 15]$.

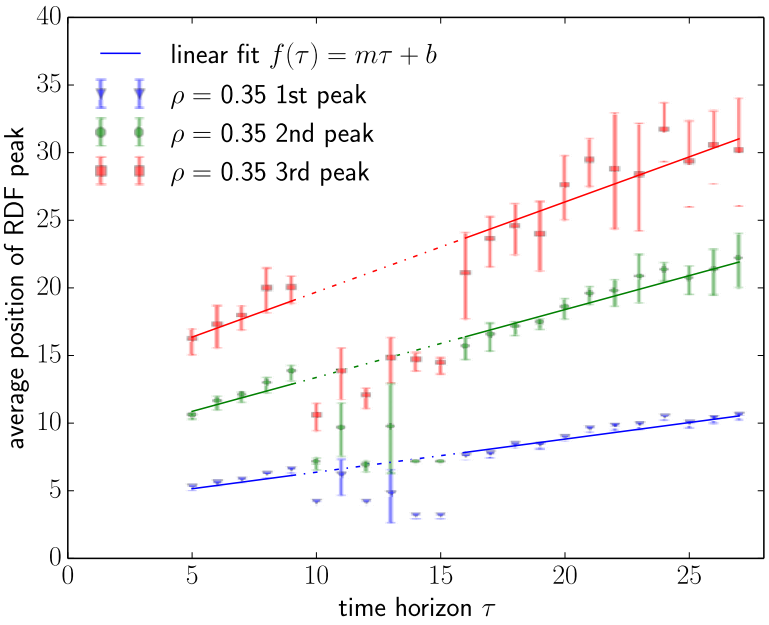

Figure 40: Dependence of RDF peak for varying $\tau \in [5, 27]$ for $s_{\text{cutoff}} = 10^6$. It shows that an increase in the number of sampling trajectories does not change the general behavior and there is no steady-state which is reached after $t_{\max} = 50$ timesteps for the range of $\tau \in [10, 15]$.

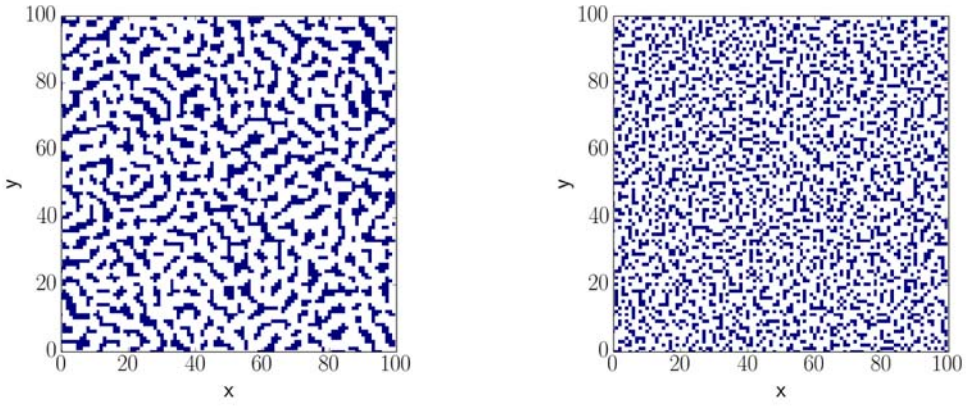

(a) (b)

Figure 41: (a) shows the steady state, after $t_{\max} = 11$ considering all sampling trajectories $s_{\text{all}} = 5^9$. (b) shows state after $t_{\max} = 200$ only considering a reduced number of sampling trajectories $s_{\max} = 10^5$, here no steady state is reached. It shows that it is due to the method of exploring only part of the phase space that pattern formation breaks down.

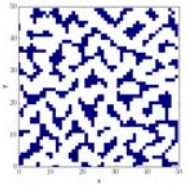

4.3.3 Comparing the approach B and C with Swift-Hohenberg model

Expanding the growth rate of the Swift-Hohenberg model Eq. (19) near the critical wave number $q_c = 1$ and for small r gives

$$\sigma_q \approx r - 4(q-1)^2 \ . \tag{25}$$

The critical parameter of the Swift-Hohenberg model is $r = 0$, which is proportional to the reduced bifurcation parameter ϵ and to the slope $m\tau_c$ near the onset of the instability hence $r = m\tau_c\epsilon$, which occurs for approach B and C at $\tau_c = 3$ and $\tau_c = 4$, respectively. Dividing Eq. (25) by the critical parameter gives

$$\frac{\sigma_q}{m\tau_c} = \epsilon - \frac{4}{m\tau_c}(q-1)^2 \ , \tag{26}$$

and rewriting Eq. (16)

$$\sigma_q \approx \frac{1}{T_0}\left[\epsilon - \xi_0^2(q-q_c)^2\right] \ . \tag{27}$$

Comparing (26) and (27) gives

$$(q_c\xi_0)^2 = \frac{4}{m\tau_c} \quad \text{and} \quad T_0 = \frac{1}{m\tau_c} \ . \tag{28}$$

From the onset on instability given by the value of τ_c, where the particle particle interaction shows a minimum at distances larger than 1, I calculate the critical wave number q_c, the typical Swift-Hohenberg time unit T_0 and the coherence length ξ_0, which are shown in Table 3. These values for T_0, ξ_0 and q_c can now be injected in Eq. (27) and simulations with this growth rate should give qualitatively comparable results.

parameter	formula	B	C
m	from Fig. 28 and 35	0.27	0.24
b	from Fig. 28 and 35	4.3	3.8
τ_c	from sec. 4.2	3	4
T_0	$(m\tau_c)^{-1}$	1.2	1.0
q_c	$2\pi(m\tau_c + b)^{-1}$	1.23	1.32
ξ_0	$\sqrt{4(m\tau_c)^{-1}}/q_c$	1.8	1.6

,

Table 3: Comparison of parameters between Swift-Hohenberg model and numerical simulations of approach B and C.

4.4 Noise

As an attempt to increase the robustness with respect to the initial conditions, I introduced noise for approach B. The normalized phase space volume for the five directions are modulated with a random noise uniformly distributed from the interval $[-\eta, \eta]$. As a measure for the robustness of the patterns the average phase space volume per particle $\langle\Omega\rangle$ is plotted in Figure 42 over time for varying levels of noise $\eta \in [0, 0.6]$, and $\tau = 8$, and $\rho = 0.3$. For all levels of noise the phase space volume per particle $\langle\Omega\rangle$ increases for the initial time steps, however the maximum $\langle\Omega\rangle$ is larger for low levels of noise, whereas for larger noise level the particles do not reach as high $\langle\Omega\rangle$. With time the noise has different influences on $\langle\Omega\rangle$. For no noise the particles reach an alternating state in less than 20 timesteps. For a very low level of noise $\eta = 0.05$ the behavior does not change a lot, since the particles cannot escape the situation where the particle is right next to another particle. This situation is examined in Figure 21; here the difference between distance 1 and distance 2 is in the range of $\Delta\Omega_{\text{p-p}} \in [0.05, 0.08]$. Depending on τ, a particle with noise $\eta < \Delta\Omega_{\text{p-p}}$ cannot overcome this barrier and hence the noise has only minor influence.

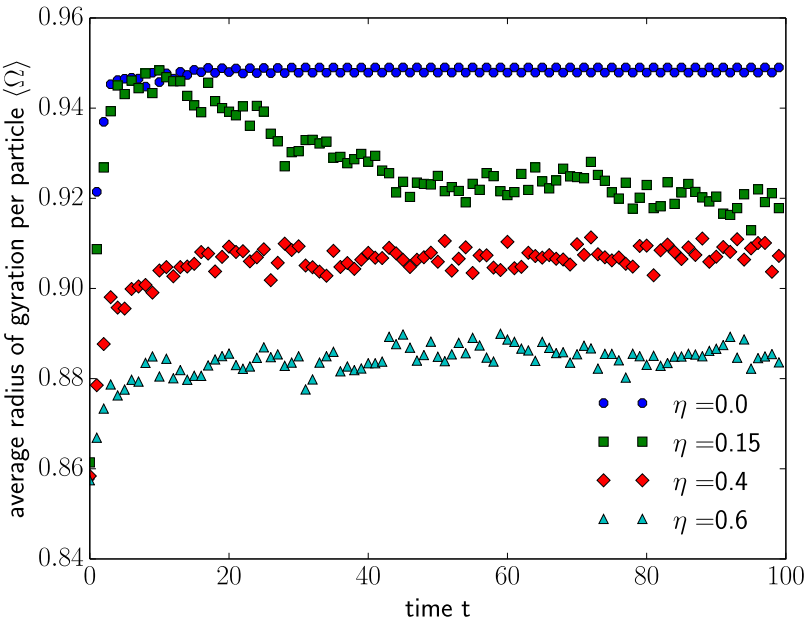

Figure 42: The evolution of the phase space volume per particle $\langle\Omega\rangle$ in time for $\tau = 8$, $\rho = 0.3$ for different levels of noise $\eta \in \{0, 0.15, 0.4, 0.6\}$ are shown. All evolutions show a increase of $\langle\Omega\rangle$ in the first 10 time steps, where the particles arrange themselves. For little level of noise the particles stay in this steady-state and hardly move or are alternating. Increasing the level of noise reduces $\langle\Omega\rangle$ since more particles become trapped in large clusters but cannot escape from this low entropy state. For high level of noise a low level of $\langle\Omega\rangle$ is reached quickly, where no patterns are present and this noisy state lasts.

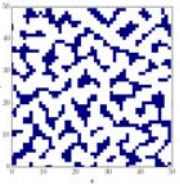

For larger values of noise $\eta \in [0.1, 0.25]$ $\langle\Omega\rangle$ decreases in time after the first increase. This can be understood by the fact that with the noise the particles move more even after they arranged themselves in the beginning, this however favours the formations of larger clusters since the particles like to be at the boundary of those clusters and the particles within the clusters cannot move away since all directions are closed with other particles. So the phase space volume Ω of the outer particles are higher but the average is lower since the particles in the middle of the cluster are in an unfavourable position and hence reduce $\langle\Omega\rangle$. For a level of noise $\eta > 0.25$ the motion is dominated by the noise and no clear patterns form. However the tendency of the particles to form patterns is hardly visible by looking at the motion, a snapshot for $t_{\max} = 200$ which is shown in Figure 43, but can still be observed in the distribution of the radial distribution function shown in Figure 44.

The influence of noise for the interaction of the particles driven by approach B is therefore counterproductive for finding a more stable pattern, since the particles move only in local ranges and the size of the cluster increases, which makes those more unstable, from a macroscopic perspective. In conclusion, introducing noise fails to find a more stable pattern fails and applying this to the more noisy approach C would result in even worse performance in building stable patterns.

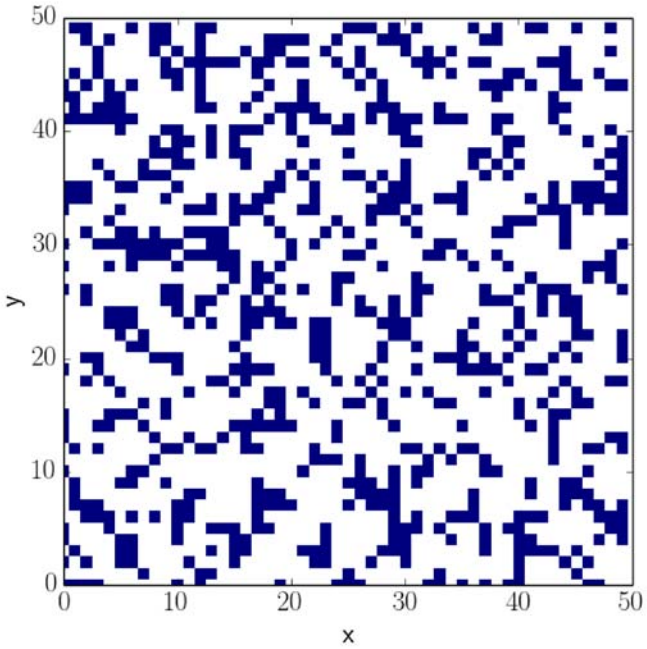

Figure 43: For a high level of noise $\eta = 0.4$ the patterns almost disappear in the noisy final state $t_{\max} = 200$ for $\tau = 8$ and $\rho = 0.3$.

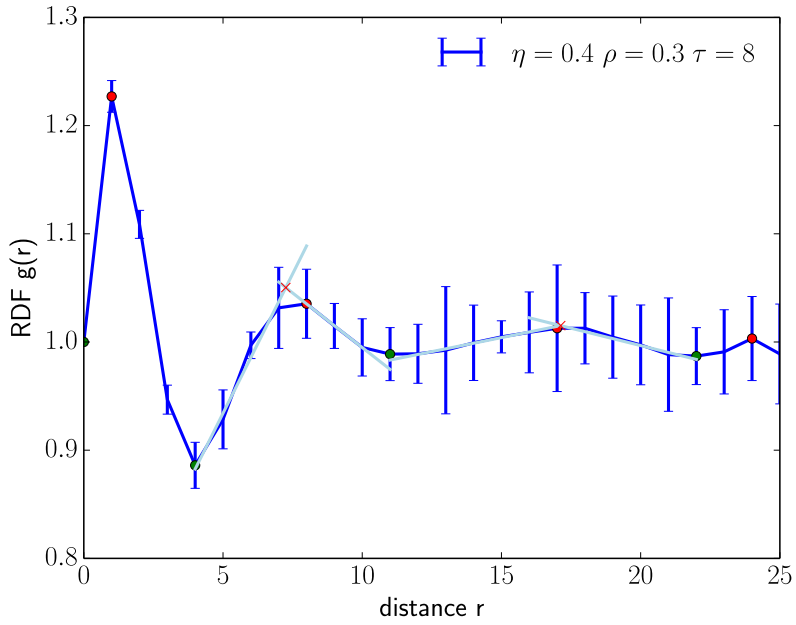

Figure 44: The tendency of the noisy system with $\eta = 0.4$ and $\tau = 8$ and $\rho = 0.3$ to build patterns can be observed through the distribution of the radial distribution function.

A different type of noise, where the particles have the possibility to jump multiple lattice sites to find other parts of the pattern and move away from local structures could have a higher chance of finding a global maximum for the phase space volume average $\langle\Omega\rangle$. Another possibility is to sample not only from the neighboring fields, but from fields with $|\boldsymbol{x}| < r_{\max}$ and use this information to generate a pressure from the particles in the center of the cluster to make it unstable. In both cases the method would change quite significantly and the simplicity of my implementation is reduced, hence I decided not to consider a variety of types of noise. Instead one could rate the stability of the pattern by the average phase space volume of the steady-state and to have an impression of more or less stable patterns one could increase the number of different initial conditions and observe the changes in steady-state with respect to the average phase space volume. Since I do not draw conclusions from single simulations but from the very robust peak of the RDF, because it is averaged over 10 different initial conditions, there is no need for me to find robust appearances of single patterns.

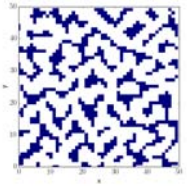

4.5 Bottleneck

The bottleneck problem was used previously by Hornischer [2] to simulate escape scenarios of intelligent agents. To explore how well his findings of continuous space can be reproduced with simulations of discrete space and time I consider this scenario in the following section.

4.5.1 Approach B

For the approach B and geometries also used in section 3.4 of a bottle's boxsize of $b = 5$ and a neck's width of $w = 1$ the first particles closest to the opening of the bottle moves to the bottle's neck, where it stays. It does so because the position right next to two walls is the ideal position of particles with the radius of gyration as a weight for the phase space volume, compare Figure 18. For all other particles the bottleneck is clogged and they cannot see the many possibilities outside of the bottle, because the sampling trajectories cannot sample past the particle in the neck. The remaining particles hence perform like in a box and form patterns within the bottle. When the width w of the bottleneck is increased the particles either form a wall in the middle of the bottleneck, as shown in Figure 45 or they partly escape and partly form patterns within the bottle. To examine the dependency of escaping particles with respect to the bottleneck's width w and to the time horizon τ Figure 46 shows the phase space of the number of escaped particles averaged over 200 runs for $w \in [1, 10]$ and $\tau \in [5, 25]$. For these simulations the size of the bottle was increased from $b = 5$ to $b = 10$, to be able for the width to range from $w = 1$ to $w = 10$. The particle density within the bottle was kept constant, which resulted in an increase of the particle number to 40 particles. Also the neck's length was kept constant throughout all simulations at $l = 3$. It shows that except for $\tau \in [10, 12]$ almost no particles escape the bottle, even through a neck with width $w = 10$, which is an open box with only three walls, almost no particles escape. I would explain the fluctuations of escapes for $\tau \in [10, 12]$ by the change of method, which was discussed in details in section 4.3.2 for the boxcount. Since only part of the phase space is explored there is noise and the particles escape more often.

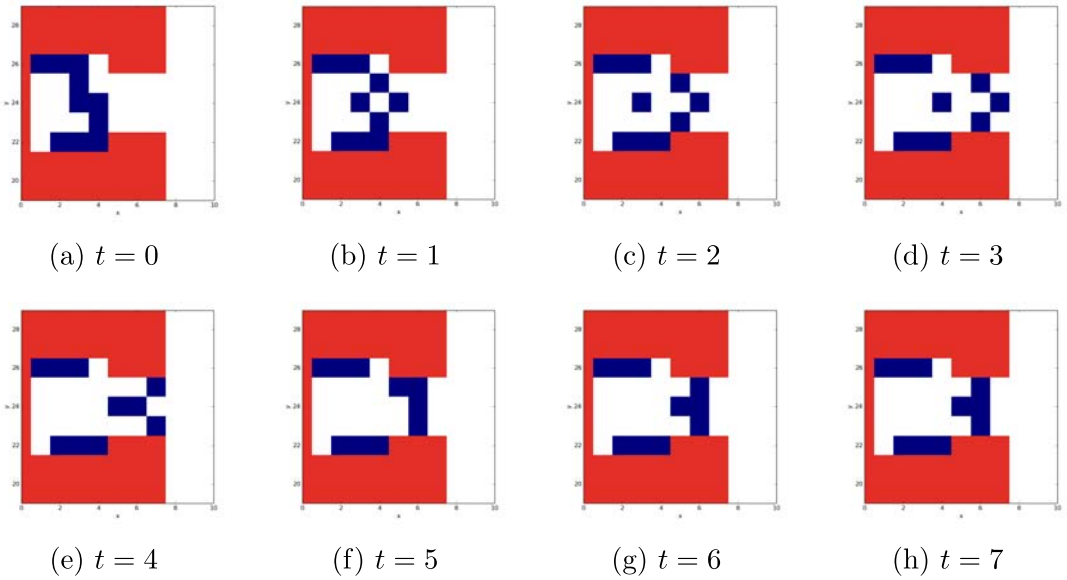

(a) $t = 0$ (b) $t = 1$ (c) $t = 2$ (d) $t = 3$

(e) $t = 4$ (f) $t = 5$ (g) $t = 6$ (h) $t = 7$

Figure 45: A typical evolution of 10 escaping particles (blue) in a bottleneck (walls in red), where $\tau = 10$, neck's length $l = 3$ and neck's width $w = 3$. Shown are the timesteps until a steady-state is reached. It shows that even for a larger width the position in the middle of the neck is so favorable that the particles build a wall and the neck is clogged.

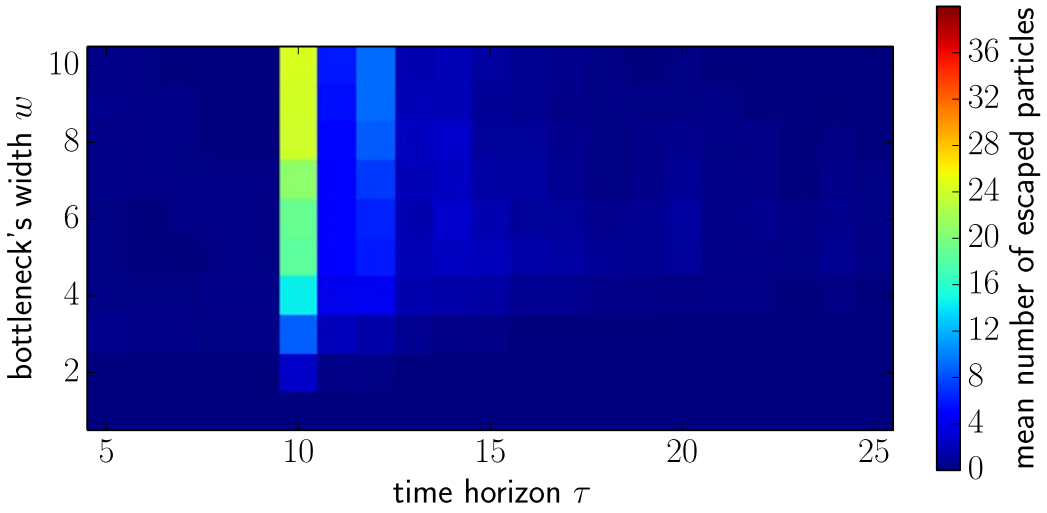

Figure 46: Phase space of the bottleneck problem with the mean number of escapes particles out of 40 averaged over 200 simulations for different neck's width $w \in [1, 10]$ and $\tau \in [5, 25]$ for constant neck's length $l = 3$. (47) shows

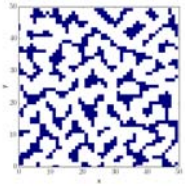

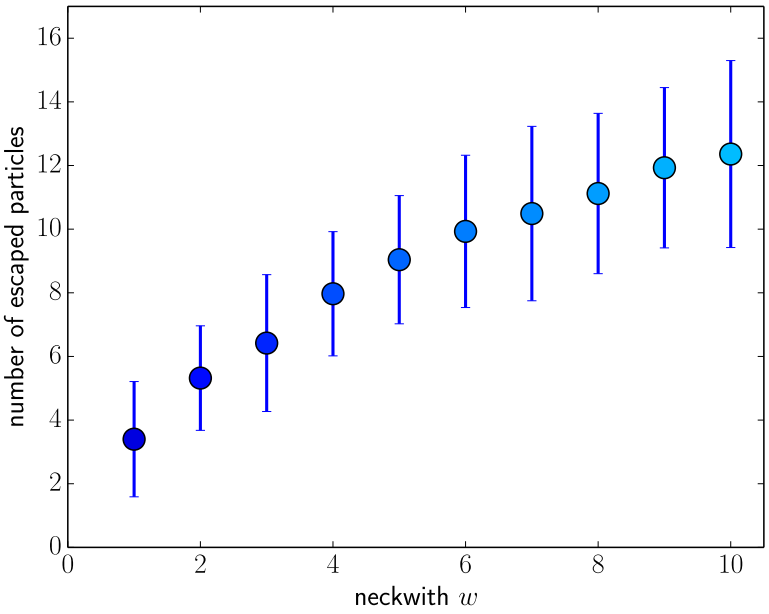

Figure 47: Mean number of escaped particles for the same scenario as Figure 46 for particles moving randomly.

4.5.2 Approach C

Turning to the approach C more particles escape the bottleneck even for neck's width of $w = 1$. Figure 49 shows the phase space of the bottleneck problem for varying length of the bottle's neck $l \in [1, 10]$ and time horizon $\tau \in [5, 25]$. It shows that for $\tau < 10$ hardly any particles escape, because two effects reduce the number of escaped particle. One is that for small τ the particles can hardly feel the size of the free space on the other side of the bottleneck, especially for larger neck's length. The second effect is that patterns form in the bottle and the particles find a local maximum of entropy, which they do not leave.

In the range of $\tau \in [10, 15]$ it shows an abrupt increase in the number of escaped particles. This can be understood looking at Figure 35, where it shows that in this range of τ no patterns form and the particles do not find a steady-state, but instead a lot of fluctuations occur. These fluctuations are the reason why more particles escape from the bottle. Comparing the number of escaped particles in Figure 49 with the number of escaped particles of randomly moving particles, which are shown in Figure 16 for the same set-up, causal-entropically driven particles perform worse in escaping the bottle than randomly moving particles. This shows that even for the noisy range of $\tau \in [10, 15]$ the level of noise is high and hence a higher number of particles escape, because of random noise, but the influence of the causal entropic force causes the particles to escape less compared to complete brownian motion.

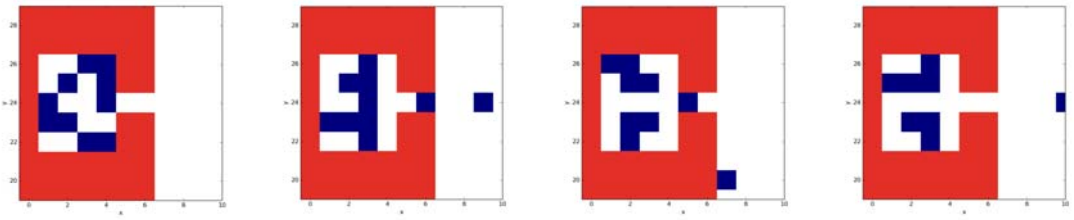

(a) $t = 0$ (b) $t = 5$ (c) $t = 10$ (d) $t = 15$

Figure 48: A typical evolution of 10 escaping particles in a bottleneck, where $\tau = 10$ and necklength $l = 2$. Shown are snapshots of the random starting condition, after 5, 10 and 15 timesteps, respectively, where a steady-state is reached and no more particles escape.

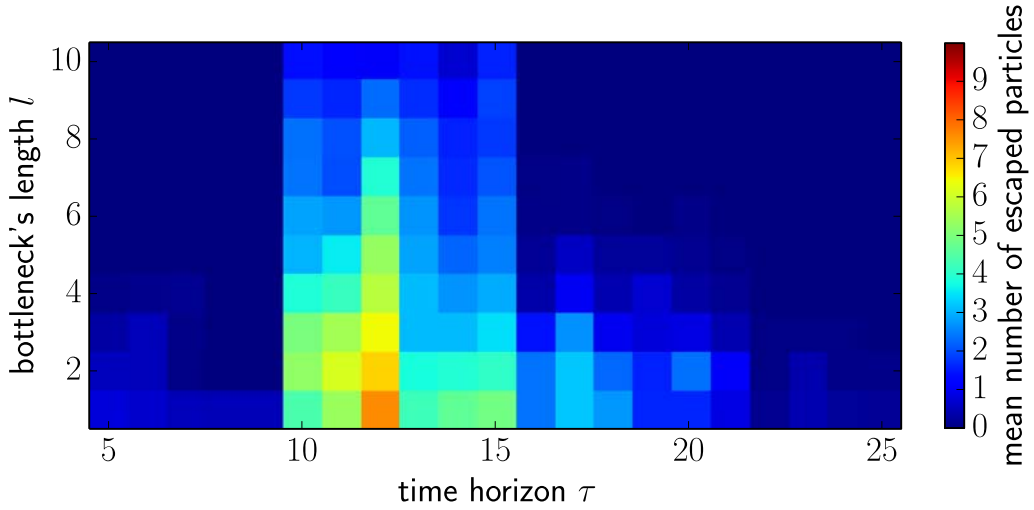

Figure 49: Phase space of the bottleneck problem with the mean number of escapes particles over 200 simulations for different necklength $l \in [1, 10]$ and $\tau \in [5, 25]$

4.5.3 Concluding the bottleneck

For the approach A of section 3.4 considering the number of trajectories for the phase space volume there is particle pressure, which results in a continuous increase of the number of escaped particles with τ (see Figure 15), since the interaction and hence the particle pressure increases.

For approach B, where the radius of gyration is used as a weight for the phase space volume the particles have a strong tendency of forming patterns and have strong interactions with other particles and walls. This results in patterns within the small box and the attraction of the walls and other particles result in a lane formation of the particles in the middle of and perpendicular to the bottleneck, which clogs it.

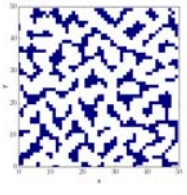

For approach C, where the boxcount is used to weigh the phase space volume, the particles behave similarly to approach B for $\tau < 10$: almost no particles escape, the neck becomes clogged and the particles form patterns within the bottle. For $\tau = 10$ the method of the algorithm changes and only a fraction of all trajectories are considered, which results in more noise of the motion, also found in section 4.3.2. This noise is the cause of an abrupt increase in the number of escaped particles at $\tau = 10$. As Figure 35 shows the patterns reappear for $\tau > 15$ and this is again the point where the number of escaped particles reduces abrupt and only few escape, caused by again a clogging of the neck and patterns in the bottle.

In conclusion, the behavior of the bottleneck for discrete space and time compared to continuous space and time studied by Hornischer [2] changed a lot, since the chance of trapping particles is much higher when there is exactly one lattice site which needs to be occupied compared to a range of positions for the continuous space, so that the particles hardly escape from the bottle. The particles behave egoistically and the position of the highest variation for future evolution with respect to the current state, or of highest diversity of future evolutions is right in the middle of the neck, where the particle can decide to move in or out. This again is supporting the statement that it is not the number of trajectories which is maximized for intelligent behavior, but the diversity or variation of state compared to the current state of future evolutions.

5 Discussion and outlook

In this thesis I examined three different approaches to quantify the phase space of possible future evolutions. Approach A considered the number of realizable trajectories as a measure. Here I found that the behavior is similar to an ideal gas, where the particles exhibit a repulsion and hence try to maximize their distance between each other. The particle pressure due to this tendency to maximize their distance is also the reason why they are escaping off a bottleneck.

The approach B where the radius of gyration, and approach C where the boxcount are considered as a weight for the sampling trajectory show very different behavior. The particles form patterns of different size, depending on the time horizon τ. Also the structure of the patterns varies from labyrinthine to polygonal, depending on density ρ and time horizon τ. The reduction of sampling trajectories to a fixed number, and hence only a fractional exploration of the phase space is the reason why the simulations for $\tau = 10$ (approach B) and $\tau \in [10, 15]$ (approach C) are noisy. Why the partial exploration of phase space causes noise only for $\tau = 10$ and $\tau \in [10, 15]$, respectively, and the robust patterns reappear for $\tau > 10$ and $\tau > 15$, respectively, is one open question, which may be answered in future work. Comparing to the results found by Hornischer for continuous space shows that the structure of the patterns varies due to the limitations of the lattice. However, a basic feature the independence of the RDF-peak with respect to ρ was also found previously. The dependence of the RDF-peak with respect to τ was not studied before, since this was very computationally expensive for continuous space and time. The comparison of the results found for approach B and C with the Swift-Hohenberg model gave rise to a deeper qualitative understanding of the causal entropic principle. Another future work could take this to the next level and examine the Swift-Hohenberg model with the suggested parameters quantitatively and compare those results with the given results of approach B and C.

The attempt to introduce noise to increase the robustness of the patterns with respect to initial conditions resulted in less robustness or a reduction of simplicity of the method, which was therefore not considered. The challenge was that trapped particles within large clusters cannot move and the low entropy state reduces the robustness but has no influence on the motion of the particles. An approach to overcome this problem and which may be studied in future work would be to sample not only from the first neighbors, but also from neighbors of higher order and use these as a foundation to implement pressure. The particles trapped in the center of a large cluster would then exert a pressure on the surrounding particles. This would probably result in a steady-state, where the pressure trying to decrease cluster sizes

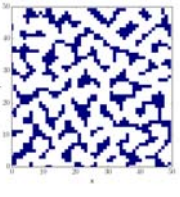

and the tendency of the particles trying to maximize cluster sizes balance.

The particle dynamics in a bottleneck for approach B and C behaves very different compared to approach A as well as results found for continuous space by Hornischer. The particles have such a high tendency to be close to walls that hardly any particles escape from the bottleneck, since they build stable patterns within the bottle. The lane formation of the escaping particles in continuous space could hence not be reproduced and the analogy for evacuation scenarios is not valid any more.

In relation to the arguments discussed in the motivation the results of this thesis show that social cooperation, i.e. pattern formation, is not reproduced when the particles interact in a way trying to maximize their number of future evolutions (approach A). Simply maximizing the number of realizable evolutions is hence not a valid theory to explain phenomena of social cooperation. For approach B and C, where the short sampling trajectories are weighted less compared to more elongated ones social cooperation or pattern formation was found. The approach B produces more robust results with respect to the fraction of phase space explored, whereas approach C, has a larger range of τ and ρ where noise is dominant. From theoretical consideration it became clear that the approach B weights short trajectories less than approach C. That the weight has an influence on the intelligence of the approach makes intuitively sense, since it is not as intelligent to go back and forth multiple times as to go in one direction for some time. Future work could therefore examine a weight for the phase space of future evolution, which does weigh short trajectories even less to find an even more robust weight. Another idea would be to implement an approach where short sampling trajectories are weighed more compared to long and see what kind of behavior follows from that.

Finally, the main goal of the thesis was achieved: to reproduce the pattern forming results of continuous space with less computational expenditure by discretizing space and time. This approach can therefore be used as a foundation for future work in the field of causal entropy maximization as an approach to explain intelligent behavior.

References

[1] A. D. Wissner-Gross and C. E. Freer, *Causal Entropic Forces*, Physical Review Letters **110**, 168702 (2013).

[2] H. Hornischer, *Causal Entropic Forces: Intelligent Behaviour, Dynamics and Pattern Formation*, Master's thesis (Georg-August University Göttingen) (2015).

[3] C. Sagan, *The Dragon of Eden - Speculation on the evolution of human intelligence*, The Random House Publishing Group (1977).

[4] T. Bertolotti, *Patterns of Rationality - Recurring Inferences in Science, Social Cognition and Religious Thinking*, Springer (2015).

[5] J. Piaget, *La naissance de l'intelligence chez l'enfant*, Fondation Jean Piaget (1936).

[6] J. Piaget, *La psychologie de l'intelligence*, Fondation Jean Piaget (1947).

[7] C. Darwin, *On the Origin of Species by Means of Natural Selection*, John Murray (1859).

[8] D. Thompson, *On Growth and Form*, Clarendon Press (1945).

[9] P. Ball, *Shapes - Nature's Patterns a tapestry in three parts*, Oxford University Press (2011).

[10] P. Ball, *The self-made tapestry: pattern formation in nature*, Oxford University Press (1999).

[11] S. Gueron and S. A. Levin, *Self-organization of Front Patterns in Large Wildebeest Herds*, Journal of Theoretical Biology **165**, 541-522 (1993).

[12] E. Tempel et al., *Detecting filamentary pattern in the cosmic web: a catalogue of filaments for the SDSS*, Monthly Notices of the Royal Astronomical Society **438**, 3465–3482 (2014).

[13] K. Fukushima, *Neocognitron: A self-organizing neural network model for a mechanism of pattern recognition unaffected by shift in position*, Biological Cybernetics **36**, 193–202 (1980).

[14] R. Bousso et al., *Predicting the Cosmological Constant from the Causal Entropic Principle*, Physical Review D **76**, 043513 (2007).

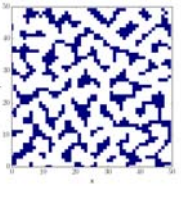

[15] L. Martyushev and V.Seleznev, *Maximum entropy production principle in physics, chemistry and biology*, Physical Reports **426**, 1 (2006).

[16] S. Gelly et al., *The grand challenge of computer Go: Monte Carlo tree search and extensions*, Association for Computing Machinery **55**, 106 (2012).

[17] M. Cross and H. Greenside, *Pattern Formation and Dynamics in Nonequilibrium Systems*, Cambridge University Press (2009).

[18] M. C. Cross and P. C. Hohenberg, *Pattern formation outside equilibirum*, Reviews of Modern Physics **65**, 851-1112 (1993).

[19] K. R. Mecke and D. Stoyan, *Statistical Physics and Spatial Statistics - The Art of Analyzing and Modeling Spatial Structures and Pattern Formation*, Springer **554** (2000).

[20] K. Malarz and S. Galam, *Square-lattice site percolation at increasing ranges of neighbor bonds*, Physical Review E **71**, 016125 (2005).